



The effect of gravity on bubble–particle collisions in turbulence

Timothy T.K. Chan¹ , Linfeng Jiang¹  and Dominik Krug^{1,2} 

¹Physics of Fluids Group, Max Planck Center for Complex Fluid Dynamics, and J. M. Burgers Centre for Fluid Mechanics, University of Twente, P.O. Box 217, 7500 AE, Enschede, The Netherlands

²Institute of Aerodynamics, RWTH Aachen University, Willnerstraße 5a, 52062 Aachen, Germany

Corresponding author: Timothy T.K. Chan, t.k.t.chan@utwente.nl; Dominik Krug, d.krug@aia.rwth-aachen.de

(Received 2 October 2024; revised 28 February 2025; accepted 21 April 2025)

Bubble–particle collisions in turbulence are key to the froth flotation process that is widely employed industrially to separate hydrophobic from hydrophilic materials. In our previous study (Chan *et al.*, 2023 *J. Fluid Mech.* **959**, A6), we elucidated the collision mechanisms and critically reviewed the collision models in the no-gravity limit. In reality, gravity may play a role since, ultimately, separation is achieved through buoyancy-induced rising of the bubbles. This effect has been included in several collision models, which have remained without a proper validation thus far due to a scarcity of available data. We therefore conduct direct numerical simulations of bubbles and particles in homogeneous isotropic turbulence with various Stokes, Froude and Reynolds numbers, and particle density ratios using the point-particle approximation. Generally, turbulence enhances the collision rate compared with the pure relative settling case by increasing the collision velocity. Surprisingly, however, for certain parameters the collision rate is lower with turbulence compared with without, independent of the history force. This is due to turbulence-induced bubble–particle spatial segregation, which is most prevalent at weak relative gravity and decreases as gravitational effects become more dominant, and reduced bubble slip velocity in turbulence. The existing bubble–particle collision models only qualitatively capture the trends in our numerical data. To improve on this, we extend the model by Dodin & Elperin (2002 *Phys. Fluids* **14**, 2921–2924) to the bubble–particle case and found excellent quantitative agreement for small Stokes numbers when the history force is negligible and segregation is accounted for.

Key words: multiphase and particle-laden flows, turbulent flows, bubble dynamics

1. Introduction

Bubble–particle collisions in turbulence are central to froth flotation, which is an industrial process widely used in different contexts such as mineral extraction and wastepaper deinking. In this process, the hydrophobic target particles, which are originally suspended in a turbulent liquid mixture, are separated through colliding with bubbles, attaching to them and being floated to the surface by the bubbles’ buoyancy. It is estimated that flotation has been used to treat 2 billion tons of ore and 130 million tons of paper annually in 2004 (Nguyen & Schulze 2004). Given the vast scale at which flotation is employed, there is a strong incentive to understand the underlying physics, model the system and improve efficiency.

Considering the multiscale nature of the problem, the bubble–particle interaction process is typically decomposed into the geometric collision rate, the collision efficiency and the attachment efficiency. These refer to the bubble–particle collision rate without accounting for the local flow disturbance caused by the bubble/particle, the correction to the collision rate due to the local flow disturbance and the probability of the particle attaching to the bubble, respectively. Since the geometric collision rate provides the baseline estimate of the bubble–particle collision rate, it will be our focus in this paper. In the literature (Pumir & Wilkinson 2016), the geometric collision rate is typically measured by the collision kernel Γ , which is related to the collision rate per unit volume by $Z_{12} = \Gamma_{12}n_1n_2$, where the subscripts 1 and 2 refer to the two colliding species and n is the number density. The collision kernel can also be expressed as a normalised particle influx across a shell whose radius is the collision distance $r_c = r_1 + r_2$ ($r_{1,2}$ are the radii of the colliding species). This shows that Γ_{12} is proportional to both the local particle density and the average approach velocity of the particles at collision distance. The former is characterised by the radial distribution function (RDF) at collision distance

$$g_{12}(r_c) = \frac{N_{pair}(r_c)/(4\pi r_c^2 \Delta r)}{N_1 N_2 / V_{box}}, \quad (1.1)$$

where $N_{pair}(r_c)$ is the number of pairs within a distance of $r_c \pm \Delta r/2$, $N_{1,2}$ is the number of particles and V_{box} is the volume of the domain; while the latter is given by the effective radial approach velocity

$$S_-^{12}(r_c) = - \int_{-\infty}^0 \Delta v_r p.d.f.(\Delta v_r | r_c) d(\Delta v_r), \quad (1.2)$$

where Δv_r is the radial component of the relative velocity, which is positive when the pair separates, and $p.d.f.(\Delta v_r | r_c)$ is the probability density function of Δv_r conditioned on a pair separated by r_c . The collision kernel is then

$$\Gamma_{12} = 4\pi r_c^2 g_{12}(r_c) S_-^{12}(r_c). \quad (1.3)$$

The value of the collision kernel can vary significantly within a real flotation cell since the turbulent flow field is highly inhomogeneous (Koh, Manickam & Schwarz 2000), which precludes the use of one simple expression to predict the overall collision rate. Typically, the flow is highly turbulent near the bottom of the flotation cell, where an impeller agitates the flow with the aim of promoting collisions between bubbles and particles. This is the region we focus on in the present study. Within this region, industrial-scale simulations divide the flow field into grids wherein subgrid-scale models are applied to determine the local bubble–particle collision rate (Koh & Schwarz 2006). These models are developed exclusively in the context of homogeneous isotropic turbulence (HIT), which has the advantage of having well-defined turbulence properties. We hence

investigated bubble–particle collisions in HIT without gravity using the point-particle approximation in our previous study (Chan, Ng & Krug 2023). Under these conditions, the most relevant parameter is the Stokes number

$$St_i = \frac{\tau_i}{\tau_\eta} = \frac{r_i^2(2\rho_i/\rho_f + 1)}{9\nu\tau_\eta}; \quad (1.4)$$

$i = 1, 2$ throughout this article and represents the colliding species. Here, $\tau_i = r_i^2(2\rho_i/\rho_f + 1)/(9\nu)$ is the particle response time (Mathai, Lohse & Sun 2020), ρ_i is the particle density, ρ_f is the fluid density, ν is the kinematic viscosity, $\tau_\eta = (\nu/\varepsilon)^{1/2}$ is the Kolmogorov time scale and ε is the average rate of turbulent dissipation. Depending on the range of St , Chan *et al.* (2023) conceptualised several collision mechanisms: at small St , collisions occur due to local fluid shear and the ‘local turnstile’ effect, i.e. bubbles and particles attain opposite slip velocities in an accelerating fluid element purely due to their density differences. For collisions due to shear, Saffman & Turner (1956) estimated the collision kernel to be $\Gamma^{(ST)} = \sqrt{8\pi/15}r_c^3/\tau_\eta$. At intermediate St , non-local effects set in as the instantaneous slip velocity is increasingly determined by the path history (Voßkuhle *et al.* 2014). Over both small and intermediate St , the collision rate is reduced by the spatial segregation between bubbles and particles. Evidently, the fact that bubbles and particles have different densities causes the problem to be fundamentally different from particle–particle collisions in turbulence. Therefore, although theories of single-density particle collisions in turbulence can be a useful reference, they must be carefully considered before being extended to the bubble–particle case.

In this study, we focus on the effect of gravity, which has to be accounted for in most realistic situations and introduces an additional non-dimensional parameter to the problem, namely the Froude number

$$Fr = \frac{a_\eta}{g}, \quad (1.5)$$

where $a_\eta = \eta/\tau_\eta^2$ and g are the turbulence and gravitational accelerations, respectively, while η is the Kolmogorov length scale. To investigate the effect of varying Fr , we conduct direct numerical simulations of bubbles and particles in HIT using the point-particle approach (Gatignol 1983; Maxey & Riley 1983; Auton 1987; Auton, Hunt & Prud’Homme 1988) and systematically vary the strength of gravity. Details on this approach will be given in § 3. As the existing bubble–particle models for the geometric collision rate are entirely based on concepts developed for the particle–particle case, we first review how gravity affects particle collisions in turbulence and then discuss the situation for bubble–particle collision in § 2. Finally, results and conclusions are presented in § 4 and § 5, respectively.

2. Theoretical framework

2.1. The effect of gravity on collisions between monodispersed particles

Even for collisions between particles with the same properties (and hence the same settling velocities), gravity is known to affect the collision rate by introducing anisotropy into the system as it only acts along the vertical direction. This has implications for the preferential sampling exhibited by the particles in turbulence. Without gravity, particles with small or moderate St deviate from the fluid pathlines and form clusters (Voßkuhle *et al.* 2014; Ireland, Bragg & Collins 2016a). This is most intuitively understood for heavy particles

using the ‘centrifuge picture’ (Maxey 1987), which suggests that the particles get expelled from regions of high rotation rate and cluster in low rotation rate and high strain rate regions. Gravity introduces an additional element to this picture by causing these particles to settle, such that they are swept by local vortical flows to preferentially sample the downward branches of vortices as they remain in the low rotation regions. As a result, their clusters are elongated in the vertical direction (Wang & Maxey 1993; Bec, Homann & Ray 2014). To be precise, this picture holds only for low St particles and other mechanisms that explain the elongation of particle clusters at higher St have been proposed (Falkinhoff *et al.* 2020). Depending on the exact St , the RDF at collision distance can either increase or decrease (Ireland *et al.* 2016*b*) relative to the no-gravity case.

Apart from changing the local particle concentration, gravity affects the collision velocity. With gravity, light and heavy particles rise and settle, respectively, which increases the particle slip velocity and reduces the time available for the particle to interact with the turbulent structures. For particles with $St \gtrsim 1$, this effect reduces S_- as the path-history effect is weakened (Ireland *et al.* 2016*b*).

2.2. The effect of gravity on collisions between particles with different response times

When the colliding particles no longer have the same response time (but still have the same density), they collide even in quiescent liquid ($Fr \rightarrow 0$) by virtue of their different settling velocities v_{T1} and v_{T2} , which are obtained by balancing drag with buoyancy in the vertical direction. In this ‘relative settling’ limit, the collision kernel is given by (Pumir & Wilkinson 2016)

$$\Gamma_{12}^{(G)} = 4\pi r_c^2 S_-^{(G)} = \pi r_c^2 |v_{T1} - v_{T2}|, \quad (2.1)$$

where the prefactor in the last equality results from the facts that collisions only occur on a hemisphere (contributing a 1/2 prefactor to $S_-^{(G)}$) and that only the radial component of the relative velocity is considered (contributing the other 1/2 prefactor to $S_-^{(G)}$).

In the intermediate Fr regime, the relative settling mechanism and turbulence are active at the same time. Several models which originally consider the no-gravity case in the very small or very large St limits (refer to Chan *et al.* (2023) for details) have been developed to incorporate relative settling. In the small St limit, Saffman & Turner (1956) approximated the probability density function (p.d.f.) of the relative velocity by a Gaussian distribution and assumed that relative settling changed the variance of the p.d.f.; however, the resulting expression fails to converge to their no-gravity limit, as acknowledged by the original authors, and gravity is included in all directions since the variance was incorrectly assumed to be isotropic. Dodin & Elperin (2002) resolved these issues by rigorously deriving the collision kernel in the small St limit to give

$$\Gamma_{12}^{(DE)} = \sqrt{8\pi} r_c^2 \sigma \left[\frac{\sqrt{\pi}}{2} \left(c + \frac{1}{2c} \right) \operatorname{erfc} + \frac{\exp(-c^2)}{2} \right], \quad (2.2)$$

where $c = |\tau_2 - \tau_1|g/(\sqrt{2}\sigma)$ and $\sigma^2 = r_c^2 \varepsilon/(15\nu) + 1.3(\tau_2 - \tau_1)^2 \varepsilon^{3/2}/\nu^{1/2}$. Crucially, they assumed that relative settling is captured by a shift in the mean vertical velocity while the variance remains unaffected. Consequently, their expression is consistent with Saffman & Turner (1956) in the no-gravity limit. In the very large St limit, where particles can be modelled as kinetic gases with normally distributed velocity components, Abrahamson (1975) similarly accounted for gravity by shifting the vertical velocity p.d.f. of each species by the mean settling velocity so that

In the high St , ‘kinetic gas-like’ limit, Bloom & Heindel (2002) adapted (2.3)–(2.5) by simply replacing the settling velocities with the bubble (particle) rising (settling) velocity, meaning

$$\alpha^{(BH)} = \frac{|v_{Tb}| + |v_{Tp}|}{\chi^{(BH)}} \quad \text{and} \quad \chi^{(BH)} = \sqrt{v_b'^2 + v_p'^2}, \quad (2.8)$$

where the subscripts b and p denote ‘bubble’ and ‘particle’, respectively. Since Bloom & Heindel (2002) incorrectly used expressions for slip velocities in lieu of v_b' and v_p' , as pointed out in Chan *et al.* (2023), in this work we employ the expression given by Abrahamson (1975) in (2.8) for both v_b' and v_p' . For intermediate St , Ngo-Cong, Nguyen & Tran-Cong (2018) first modelled the zero-gravity bubble–particle velocity correlation following the approach of Yuu (1984), such that the root mean square (r.m.s.) of the single-component bubble–particle relative velocity without gravity is $\sigma_{\Delta v}^{(NC)} = [(A_b + A_p - 2B)u'^2 + (A_b r_b^2 + A_p r_p^2 + 2B r_p r_b)\varepsilon/(9\nu)]^{1/2}$, where u' is the single-component r.m.s. fluid velocity fluctuation, and A_i and B are coefficients that depend on particle properties and the fluid Lagrangian integral time scale. They then included gravity using (2.4) with

$$\alpha^{(NC)} = \frac{|v_{Tb}| + |v_{Tp}|}{\chi^{(NC)}} \quad \text{and} \quad \chi^{(NC)} = \sigma_{\Delta v}^{(NC)}. \quad (2.9)$$

We point out that (2.4) is derived from (2.3), which assumes uncorrelated particle velocities. The use of (2.4) at intermediate St , where the correlation between particle velocities remains finite, is therefore inconsistent. In addition, both Bloom & Heindel (2002) and Ngo-Cong *et al.* (2018) use the wrong integration result (2.4), such that these models also do not converge to the correct no-gravity limit. Expressions that have been corrected for this error are given by (2.6) and (2.7), along with (2.8) for Bloom & Heindel (2002) and (2.9) for Ngo-Cong *et al.* (2018). For small St , a consistent model for bubble–particle collisions in turbulence with gravity is missing to date. We extend the theory by Dodin & Elperin (2002) to the bubble–particle case (see Appendix B for details) and include a drag correction f_i ($f_i = 1$ for Stokes drag) to obtain

$$\Gamma_{bp}^{(DEX)} = \sqrt{8\pi} r_c^2 \sigma_{\Delta vr}^{(DEX)} \left[\frac{\sqrt{\pi}}{2} \left(c + \frac{1}{2c} \right) \text{erfc} + \frac{\exp(-c^2)}{2} \right], \quad (2.10)$$

where

$$\sigma_{\Delta vr}^{(DEX)} = \sqrt{\frac{r_c^2 \varepsilon}{15\nu} + 1.3 \left(\frac{\beta_b \tau_b}{\langle f_b \rangle} - \frac{\beta_p \tau_p}{\langle f_p \rangle} \right)^2 \frac{\varepsilon^{3/2}}{\nu^{1/2}}} \quad (2.11)$$

is the r.m.s. of Δv_r in zero gravity, $\beta_i = 2(\rho_f - \rho_i)/(\rho_f + 2\rho_i)$,

$$c = \frac{|\beta_b \tau_b / \langle f_b \rangle - \beta_p \tau_p / \langle f_p \rangle| g}{\sqrt{2} \sigma_{\Delta vr}^{(DEX)}} \quad (2.12)$$

is the ratio of the relative settling velocity to the turbulence-induced radial collision velocity (up to a constant) and $\langle \cdot \rangle$ denotes averaging. This expression incorporates three collision mechanisms at small St : collision due to local fluid shear, local turnstile mechanism and relative settling. We note that Kostoglou *et al.* (2020a) proposed a model which considers a bubble in a swarm of tracers. However, since it does not decompose the

Re_λ	N	$\bar{\epsilon}$	η	$k_{max}\eta$	u_η	u'/u_η	u'_x/u'_y	T_L/τ_η	$N_{b,p}$
69	256 ³	51.9	0.0042	3.4	0.60	4.2	0.99	18	10 000
167	512 ³	356	0.0013	2.1	0.77	6.6	0.95	43	77 700 – 140 000

Table 1. Statistics of HIT: the grid size (N), pseudo-dissipation ($\bar{\epsilon}$), Kolmogorov length scale (η), maximum wavenumber (k_{max}), Kolmogorov velocity (u_η) scale, r.m.s. velocity fluctuations (u'), large-scale isotropy (u'_x/u'_y) and the large eddy turnover time (T_L) relative to the Kolmogorov time scale (τ_η). Here, $N_{b,p}$ are the numbers of bubbles and particles, respectively. The simulations including the history force have the same parameters as the $Re_\lambda = 167$ case except for a lower number of bubbles and particles $N_{b,p} = 50\,000$.

collision process into the geometric collision rate and the collision efficiency, we do not further consider it in this study.

While several models for bubble–particle collisions in turbulence that account for gravity are available, none of them have been directly tested. Even in zero gravity, the model predictions are hugely different from simulation results, which underscores the lack of understanding and the richness of the physics of bubble–particle collisions (Chan *et al.* 2023). The only direct numerical study on bubble–particle geometric collisions with gravity in HIT that we are aware of does not vary St , Fr and Re_λ independently (Wan *et al.* 2020). The goal this work is therefore to systematically investigate the effect of St , Fr and Re_λ for bubble–particle collisions through simulations in order to reveal the underlying physical picture and assess the available models.

3. Methods

The simulations are performed using the same fluid and particle solvers as Chan *et al.* (2023). Hence, we only provide a brief summary here for completeness. For the background turbulence, we run direct numerical simulations of HIT using a finite-difference solver (second order in space, third order in time) to solve the incompressible Navier–Stokes and continuity equations

$$\frac{D\mathbf{u}}{Dt} = -\frac{1}{\rho_f}\nabla P + \nu\nabla^2\mathbf{u} + \mathbf{f}\psi, \tag{3.1a}$$

$$\nabla \cdot \mathbf{u} = 0, \tag{3.1b}$$

where D/Dt is the material derivative following a fluid element, \mathbf{u} is the fluid velocity, t is the time and P is the pressure. The fluid is forced randomly at the largest scales $\mathbf{f}\psi$ using the scheme by Eswaran & Pope (1988) to generate turbulence with $Re_\lambda = 69$ and 167. Other turbulence statistics are displayed in table 1. We also show in figure 1 that the power spectrum agrees excellently with that of Jiménez *et al.* (1993).

For the bubbles and particles, we approximate them using the point-particle approach (for a historical overview of this approach, see Michaelides 2003) which implies that both species are modelled as rigid spheres. This is reasonable even for the bubbles since the Weber number based on their rise velocity at $(St_b, 1/Fr, Re_\lambda) = (11, 4.4, 64)$ is $O(0.1)$ (Jiang & Krug 2025). As described later in this section, this work focuses on bubbles with lower values of St_b , such that the bubble radii and rise velocities are smaller at comparable values of $1/Fr$, thus bubble deformation is even less significant. Under the point-particle approach (Gatignol 1983; Maxey & Riley 1983; Auton *et al.* 1988), the net force on the particle is the sum of the drag force, the pressure gradient force, the added mass force, buoyancy, lift (Auton 1987), the history force and Faxén terms. We initially neglect the history force and Faxén terms to allow fair comparison with the models introduced

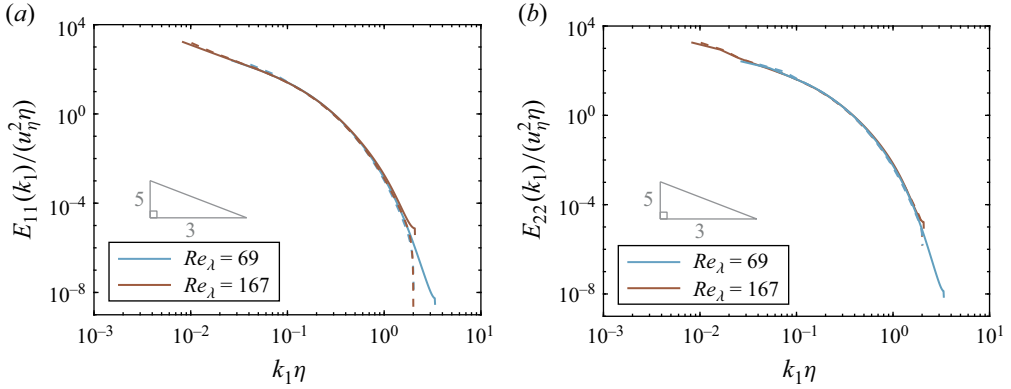


Figure 1. The (a) longitudinal and (b) transverse energy spectra. The dashed lines show data from Jiménez *et al.* (1993) for $Re_\lambda = 62.7$ (in blue) and 170.2 (in brown).

in § 2.3. A finite-difference solver is used to solve

$$\begin{aligned} \frac{4}{3}\pi r_i^3 \rho_i \frac{d\mathbf{v}_i}{dt} &= 6\pi\mu r_i f_i(\mathbf{u} - \mathbf{v}_i) + \frac{4}{3}\pi r_i^3 \rho_f \frac{D\mathbf{u}}{Dt} + \frac{2}{3}\pi r_i^3 \rho_f \left(\frac{D\mathbf{u}}{Dt} - \frac{d\mathbf{v}_i}{dt} \right) \\ &+ \frac{4}{3}\pi r_i^3 (\rho_f - \rho_i) g \mathbf{e}_z - \frac{2}{3}\rho_f \pi r_i^3 (\mathbf{v}_i - \mathbf{u}) \times \boldsymbol{\omega}, \end{aligned} \quad (3.2)$$

where \mathbf{v}_i is the particle velocity, $\mu = \nu\rho_f$ is the absolute viscosity, \mathbf{e}_z is the unit vector pointing vertically upwards, $\boldsymbol{\omega}$ is the vorticity vector and $f_i = 1 + 0.169Re_i^{2/3}$ is the correction factor that accounts for nonlinear drag due to finite bubble or particle Reynolds number $Re_i = 2r_i|\mathbf{u} - \mathbf{v}_i|/\nu$ and implies a no-slip boundary condition (Nguyen & Schulze 2004). Here, r_i is determined from (1.4), while \mathbf{u} , $D\mathbf{u}/Dt$ and $\boldsymbol{\omega}$ at the particle positions are evaluated using tri-cubic Hermite spline interpolation with a stencil of four points per direction (van Hinsberg *et al.* 2013). We employ a lift coefficient C_L of 1/2, which strictly speaking is only valid for clean bubbles with very large Re_b in simple shear flows (Auton 1987; Legendre & Magnaudet 1998), and acknowledge that the actual value depends on the type of flow and Re_b (Legendre & Magnaudet 1998; Magnaudet & Legendre 1998). Nonetheless, we use $C_L = 1/2$ following Mazzitelli & Lohse (2004), who simulated similar bubbles in HIT. Although we initially neglect the history force, we recognise that it may play a noticeable role in reality for our tested bubble and particle density ratios (Olivieri *et al.* 2014; Daitche 2015). We therefore run additional cases in § 4.5 with the history force

$$\mathbf{F}_{hist} = 6r_i^2 \rho_f \sqrt{\pi\nu} \int_0^t \frac{d(\mathbf{u}(\tau) - \mathbf{v}_i(\tau))}{d\tau} \frac{d\tau}{\sqrt{t - \tau}} \quad (3.3)$$

added to the right-hand side of (3.2). The value of \mathbf{F}_{hist} is computed using the semi-implicit scheme by van Hinsberg, ten Thije Boonkamp & Clercx (2011), where a window length of 5 time steps is chosen and the tail of the integrand is modelled with 10 exponential functions. Hence, the results are comparable to a simple window method (Dorgan & Loth 2007) where the integration is truncated to the last 500 time steps (van Hinsberg *et al.* 2011). This corresponds to approximately $9\tau_\eta$, which Calzavarini *et al.* (2012) found is long enough for the integrand to decay to negligible values in HIT for their parameters.

In all our simulations, the collisions are treated using the ‘ghost collision’ scheme as it is consistent with the models described in § 2 (Wang, Wexler & Zhou 1998). This

means particles can overlap and a collision is registered every time an approaching pair of particles reaches the collision distance r_c , which is set to $r_b + r_p$ for all species. We eliminate wall effects by implementing periodic boundary conditions in all directions and verified that the domain size $L_{box} = 1$ is sufficiently large to minimise periodicity effects (see Appendix C). The time step $\Delta t \leq \tau_\eta/55$ is sufficiently small such that the Courant–Friedrichs–Lewy (CFL) number ≤ 1 (apart from a few time steps for the cases in §§ 4.4 and 4.5) and the point-particle statistics are no longer sensitive to Δt (Ruth *et al.* 2021). We refer the reader to Chan *et al.* (2023) for details of the solvers and the collision detection algorithm.

We investigate bubbles ($\rho_b/\rho_f = 1/1000$) and particles ($\rho_p/\rho_f = 5$) with St of 0.1, 0.5, 1, 2 and 3, and $1/Fr$ ranging from 0.01 to 10. For the bubbles, these values of St correspond to $r_b/\eta = 0.9, 2.2, 3.0, 4.2$ and 5.2 , respectively; and it should be noted that finite-size effects, that are not represented in our computations, may become relevant in particular at the larger values of St . Nonetheless, we believe that our approach still allows us to examine the general trend with increasing St and to assess the collision models introduced in § 2.3, which also do not include these effects. We consider only $St_b = St_p$ to limit the parameter space. While this is not the most general case, it is physically relevant, especially in the context of flotation of fine particles, where small bubbles are preferred (Ahmed & Jameson 1985; Miettinen, Ralston & Fornasiero 2010; Farrokhpay, Filippov & Fornasiero 2021). The simulation is conducted as follows: bubbles and particles, 10 000–140 000 per species, are injected in the simulation domain at random positions after the flow has reached statistical stationarity. We then monitor the particle position p.d.f., particle velocity p.d.f. and the ensemble-average rise/settling velocities to identify transients. Once the transient states have passed, we collect statistics over at least 12.4 large eddy turnover times (T_L) at a minimum sampling frequency of once per $0.06T_L$.

4. Results

4.1. Collision kernel

Figure 2(a) presents results for the bubble–particle collision kernel normalised by the relative settling case in still fluid $\Gamma^{(G)}$, wherein the terminal velocities v_{Ti} are obtained by balancing buoyancy with the nonlinear drag term as shown by (3.2). At small $1/Fr$ (weak gravity), $\Gamma/\Gamma^{(G)}$ is large since bubbles and particles rise and settle very slowly such that $\Gamma^{(G)}$ is small and the collision rate is dominated by turbulence mechanisms. In this regime, $\Gamma/\Gamma^{(G)}$ reduces with increasing St primarily because the rise and settling speeds $|v_{Ti}|$ are proportional to St . As $1/Fr$ increases, bubbles and particles rise and settle faster, enhancing the role of relative settling in the overall collision rate as reflected by a decreasing $\Gamma/\Gamma^{(G)}$ such that, at large $1/Fr$, $\Gamma \approx \Gamma^{(G)}$. At close inspection, however, $\Gamma < \Gamma^{(G)}$ when $1/Fr \gtrsim 5$ for $St = 0.1$ and $1/Fr \gtrsim 1$ for $St \geq 0.5$, as shown in the inset. This implies that, counter-intuitively, the presence of turbulence decreases the collision rate below the relative settling case in this regime. This is attributed to the non-uniform bubble–particle spatial distribution and their resulting segregation, and to the reduced bubble slip velocity due to nonlinear drag, as will be discussed further in §§ 4.2 and 4.3. As the segregation does not monotonically depend on St , there is no simple dependence between $\Gamma/\Gamma^{(G)}$ and St in this regime. Throughout the tested range of $1/Fr$ and Re_λ , $\Gamma/\Gamma^{(G)}$ is not sensitive to Re_λ .

All the models considered successfully capture the general decreasing trend of $\Gamma/\Gamma^{(G)}$ and the relative settling limit $\Gamma \rightarrow \Gamma^{(G)}$ at $1/Fr \rightarrow \infty$. However, the model predictions

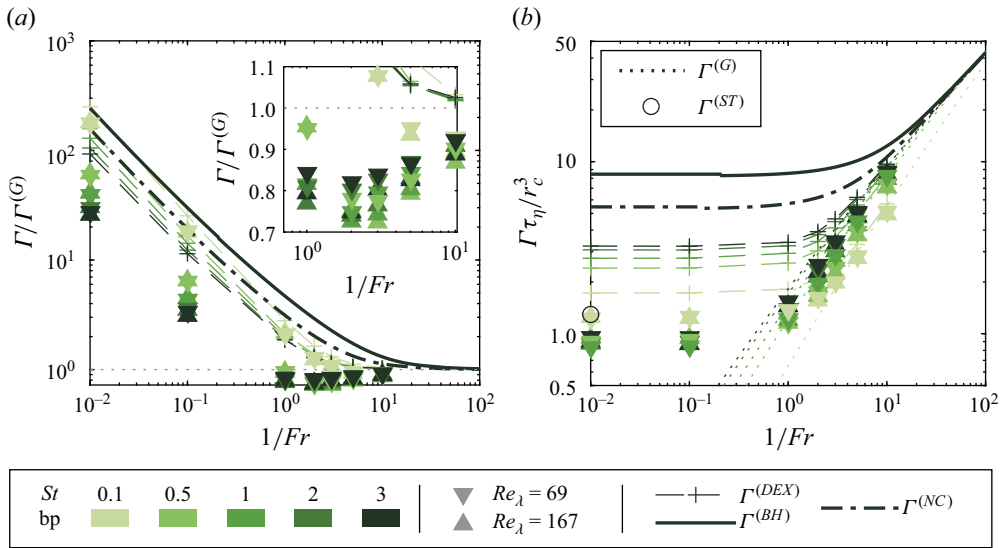


Figure 2. (a) The bubble–particle collision kernel normalised by the result for the relative settling case in still fluid. The inset shows a close-up view of the region where $1/Fr \geq 1$. (b) The bubble–particle collision kernel normalised by r_c^3/τ_η . Here, $\Gamma^{(BH)}$ and $\Gamma^{(NC)}$ (only shown for $St = 3$) are computed using the corrected best-fit (2.7). The model predictions are for $Re_\lambda = 167$.

remain above $\Gamma^{(G)}$ over the entire range of $1/Fr$ even though the nonlinear drag expression has already been included. This is because they assume a uniform bubble–particle distribution and employ the bubble rise velocity in still fluid. As mentioned at the end of the last paragraph, this is not true from the simulations and will be elaborated on in §§ 4.2 and 4.3.

We now normalise the collision kernel by τ_η/r_c^3 , i.e. the scaling of $\Gamma^{(ST)}$, in figure 2(b) to better examine the turbulence-to-relative settling transition. When $1/Fr \lesssim 0.1$, bubble and particle dynamics is turbulence dominated and the results are consistent with Chan *et al.* (2023): the collision kernel coincides with $\Gamma^{(ST)}$ at small St and $\Gamma^{(NC)}$ and $\Gamma^{(BH)}$ overpredict the collision kernel. We stress, however, that the agreement with $\Gamma^{(ST)}$ is merely a coincidence since the model does not account for bubble–particle segregation, as discussed in Chan *et al.* (2023). When $1/Fr$ increases, the effect of gravity on the collision kernel becomes noticeable and causes it to increase towards $\Gamma^{(G)}$. In the tested parameter range, Γ is only weakly sensitive to Re_λ . Among the models, $\Gamma^{(DEX)}$ best matches the data for the parameters investigated. This is expected since it has been developed for the small St limit and has been extended to the bubble–particle case to also incorporate the local turnstile mechanism. On the other hand, Bloom & Heindel (2002) is applicable for the large St kinetic gas limit which is inaccessible with the point-particle approach. Nonetheless, even for the $St = 0.1$ case $\Gamma^{(DEX)}$ does not quantitatively agree with the data, presumably due to preferential sampling, as will be examined in the following section.

4.2. Bubble–particle distribution

In zero gravity, bubbles and particles with small or moderate St preferentially sample different flow regions in HIT due to different relative densities and form respective clusters at regions of high and low rotation rates, meaning they segregate (Calzavarini *et al.* 2008). This effect has been shown to be most pronounced at $St = 1$ (Chan *et al.* 2023). To examine

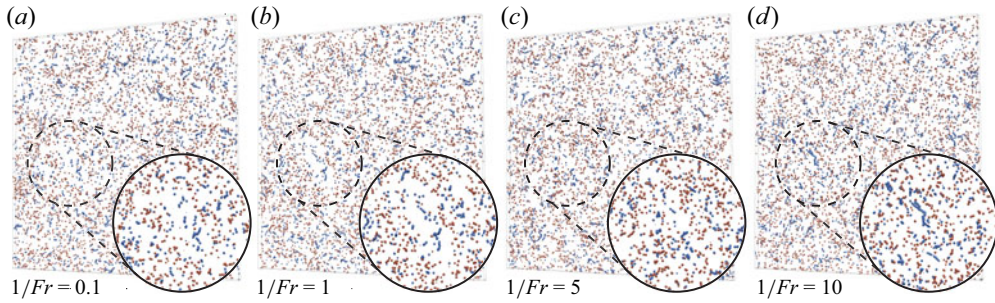


Figure 3. Instantaneous snapshots of bubbles (blue) and particles (red) in a slice with width \times height \times depth $= L_{box} \times L_{box} \times 20\eta$ with $Re_\lambda = 167$, $St = 1$ and (a) $1/Fr = 0.1$, (b) $1/Fr = 1$, (c) $1/Fr = 5$ and (d) $1/Fr = 10$. Gravity is directed vertically downwards. The sizes of the bubbles and particles are not to scale.

the effect of gravity on the spatial distribution of bubbles and particles, [figure 3](#) displays the instantaneous snapshots of the simulation with $St = 1$ over a range of $1/Fr$. As $1/Fr$ becomes larger, the overlap between bubble and particle positions increases. However, we do not observe a clear elongation of the bubble and particle clusters in the vertical direction, in contrast to other studies of heavy particles in turbulence ([Bec *et al.* 2014](#); [Ireland *et al.* 2016b](#); [Falkinoff *et al.* 2020](#)). This is because these studies employed a higher ρ_p , which enhances the overall effect of gravity. To more quantitatively investigate the locations sampled by bubbles and particles, we consider the theory by [Bec *et al.* \(2014\)](#), which predicts that a negative horizontal divergence of \mathbf{v}_p occurs on average in downward flows when particles are settling in turbulence, i.e. ‘preferentially sweeping’ ([Wang & Maxey 1993](#)). Extending this reasoning to buoyant bubbles would mean that bubbles also cluster in downflow regions. Furthermore, the lift force pulls rising bubbles toward the downward branches of vortices ([Mazzitelli, Lohse & Toschi 2003](#)). Collectively, this implies bubbles and particles sample downward flows in turbulence due to gravity. We test this hypothesis by plotting the mean vertical fluid velocity at bubble and particle positions in [figure 4\(a\)](#) and show that this is indeed the case for $St/Fr \gtrsim 10^{-1}$, with bubbles sampling regions with stronger downflow than particles. Additionally, the figure shows that $\langle u_z \rangle_i$ collapses especially for $St \geq 0.5$ when plotted against St/Fr , which echoes the finding by [Good *et al.* \(2014\)](#) that St/Fr is a key indicator of different particle settling regimes. To single out the colliding bubbles and particles, we condition the fluid velocity on pairs that are close to the collision distance in [figure 4\(b\)](#). We observe that the colliding pairs also preferentially sample downflow regions, and $\langle u_z \rangle_i|_{col}$ essentially takes the unconditioned bubble values $\langle u_z \rangle_b$. This suggests that the bubble–particle collisions occur mainly at the unconditioned bubble positions such that the collision rate depends on the location of the particle clusters relative to the bubbles. To further examine this, we plot the norm of the rotation rate $\langle R^2 \rangle$ at bubble and particle positions in [figure 4\(c\)](#). When gravity is weak, bubbles and particles preferentially sample regions with high and low $\langle R^2 \rangle$ values, respectively. As gravity becomes stronger, the values of both particle and (to a lesser extent) bubble $\langle R^2 \rangle$ begin to return to the tracer limit of 0.5, which indicates a change in the clustering location and/or bubbles and particles cluster less.

To directly measure the overall effect of preferential sampling on the collision kernel, we compute the RDF at collision distance $g(r_c)$, which reflects the probability of finding a particle at a distance r_c from another particle relative to a uniform distribution. In short, $g(r_c) < 1$ and > 1 indicate segregation and clustering, which respectively either decreases or increases the collision rate based on (1.3). [Figure 5\(a\)](#) shows $g(r_c)$ as a function of St/Fr . Focusing on the lowest $1/Fr$ case when gravity is still weak, bubbles

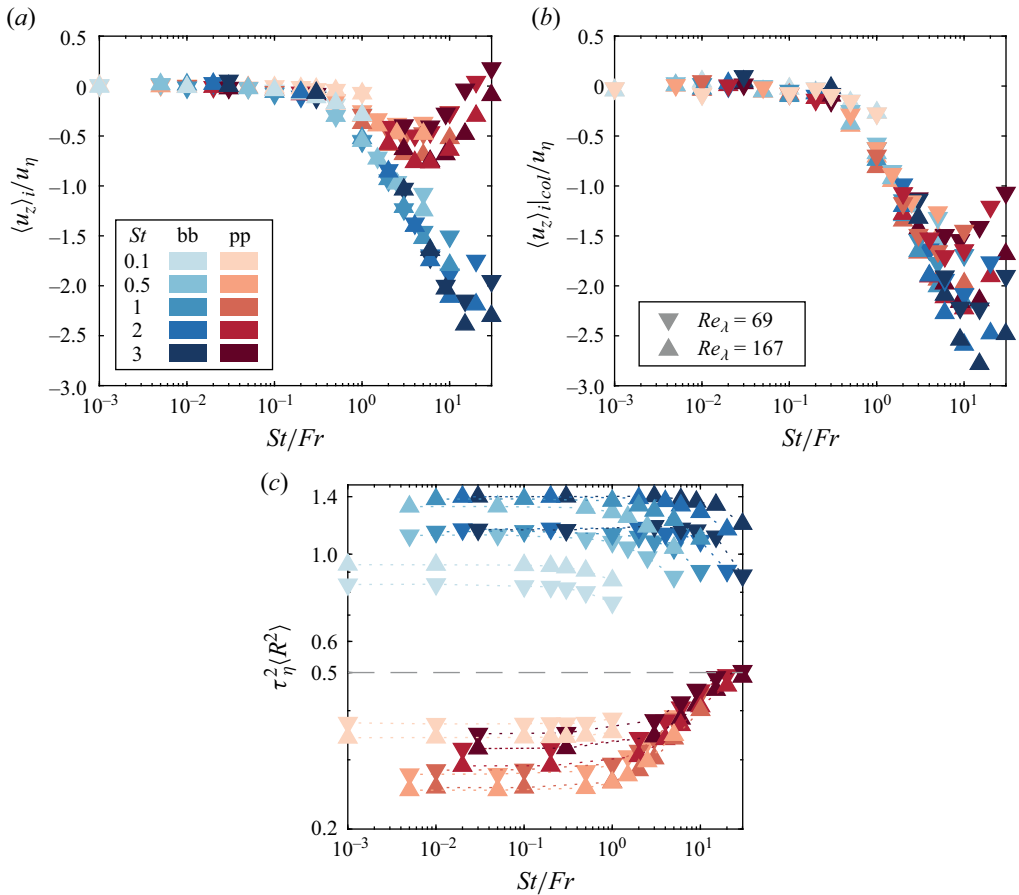


Figure 4. (a) Mean vertical fluid velocity at bubble and particle positions plotted against St/Fr . (b) Same as (a) but conditioned on pairs with $r \in [r_c - 0.1\eta, r_c + 0.1\eta]$. (c) The norm of the rotation rate of the flow at bubble and particle positions. The lines are guides for the eye.

and particles form their own clusters so $g_{bb}(r_c)$ and $g_{pp}(r_c) > 1$. However, since bubbles and particles individually cluster at different regions of the flow owing to their different relative densities, they segregate and $g_{bp}(r_c) < 1$. The segregation is strongest at $St = 1$ when $g_{bp}(r_c)$ reaches its lowest value, which is consistent with the no-gravity case (Chan *et al.* 2023). As $1/Fr$ increases, the extent of segregation reduces and eventually reaches $g_{bp}(r_c) = 1$. We note that $g_{bp}(r_c)$ for $St \geq 0.5$ collapses when plotted against St/Fr as shown in figure 5(a). This may be because particle clusters are affected by preferential sampling (Wang & Maxey 1993), which scales as St/Fr as shown in figure 4(a). Curiously, neither $g_{bb}(r_c)$ nor $g_{pp}(r_c)$ reaches 1 even at the largest tested value of St/Fr , which indicates that reduced bubble or particle clustering is not the primary cause of the reduced segregation. On closer inspection, $g_{bp}(r_c)$ for $St \geq 0.5$ already deviates noticeably from the $1/Fr \rightarrow 0$ limit in the range $10^{-1} \lesssim St/Fr \lesssim 10^0$ despite $g_{pp}(r_c)$ and $g_{bb}(r_c)$ remaining mostly constant, i.e. bubbles and particles still cluster as strongly as before. From figure 4(c), in this range of St/Fr , the value of the bubble $\langle R^2 \rangle$ already decreases for $St = 0.5$ and the value of the particle $\langle R^2 \rangle$ already increases for $St \geq 1$. This suggests the bubbles and particle clusters migrate closer together, which would increase $g_{bp}(r_c)$. For the tested parameters, $g_{bp}(r_c)$ is not sensitive to Re_λ . To account for segregation in the model

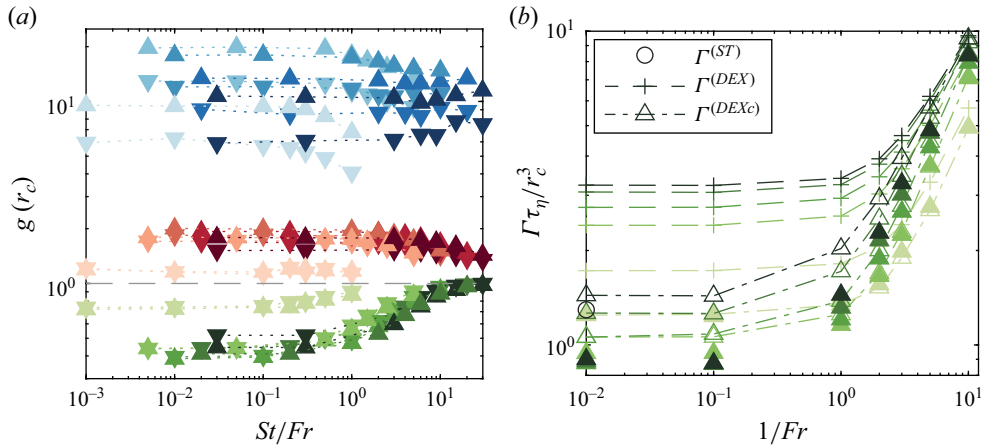


Figure 5. (a) The RDF at collision distance $g(r_c)$. Only 25% of all the bubbles were considered when computing $g_{bb}(r_c)$. (b) The collision kernel and the prediction of the extended Dodin & Elperin (2002) model after compensating for $g(r_c)$ plotted against $1/Fr$ for $Re_\lambda = 167$. The lines are guides for the eye. The symbols and colour scheme follow figures 2 and 4.

by Dodin & Elperin (2002), we multiply $g_{bp}(r_c)$ to $\Gamma^{(DEX)}$ to obtain $\Gamma^{(DEXc)}$, which is plotted in figure 5(b). As anticipated, $\Gamma^{(DEXc)}$ agrees excellently with the simulation data at the lowest St , indicating that the model correctly represents the relevant physics when corrected for the effect of segregation.

As gravity introduces anisotropy in the vertical direction, we further quantitatively examine the bubble–particle spatial distribution by binning the RDF by the polar angle to obtain the angular distribution function (ADF) (Gualtieri, Picano & Casciola 2009; Ireland *et al.* 2016b), which is normalised by the RDF in figure 6. We have $ADF/g_{bp}(r) \neq 1$ everywhere when gravity is included, as expected (Ireland *et al.* 2016b). Intriguingly, particles preferentially sample the regions directly above bubbles, especially when St/Fr becomes sufficiently large. To understand this, we consider figure 4(a), which showed that bubbles and particles preferentially sample downflows, and examine the local flow structure by overlaying the ADF on top of the azimuthally averaged flow field around the bubble in a reference frame where the mean vertical flow velocity in the sampled region is zero in figure 6. The results show that there are vortices with their downward branches passing the bubble and the region where the flow converges horizontally corresponds to the locations with higher particle concentration, suggesting that the convergent flow influences the particle trajectories such that they are concentrated above bubbles. In the cases with appreciable anisotropic particle distributions (i.e. $St = 1, 3$ and $1/Fr \geq 1$), the vertical component of the flow velocity vector at the bubble position, as displayed in figure 6, amounts to 60%–80% of $\langle u_z \rangle_b$ and decreases very slightly as $1/Fr$ increases. Despite the local flow field contributing less to $\langle u_z \rangle_b$ with increasing $1/Fr$, the particle distribution is most anisotropic at intermediate $1/Fr$ since the particles settle faster at large $1/Fr$, meaning they will have less time to interact with the background turbulence such that they will be more isotropically distributed. For the tested parameters, this anisotropy increases with St . Nonetheless, we expect that it is strongest for some finite St and weakens as St becomes very large when the particles no longer respond to the background flow. Overall, this means that collisions will occur more frequently on top of a bubble at intermediate $1/Fr$ and St even without considering the azimuthal variation of the collision velocity due to gravity.

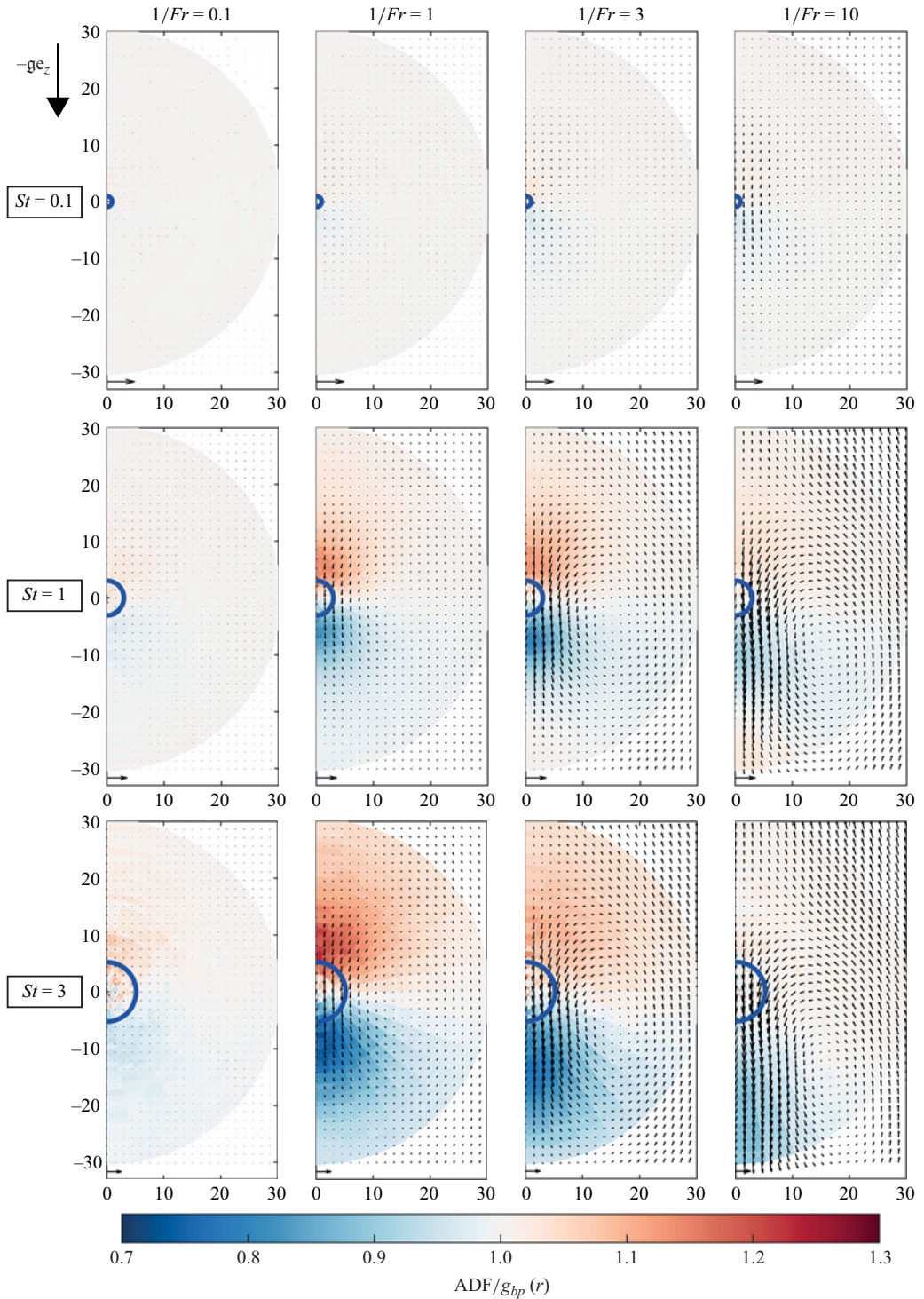


Figure 6. The ADF at different distances and the azimuthally averaged local flow field in a reference frame where the mean vertical flow velocity in the sampled region is zero. Here, $Re_\lambda = 167$. The semicircle and the reference arrow on the bottom row indicate the bubble and u_η , respectively. The axis labels are in units of η .

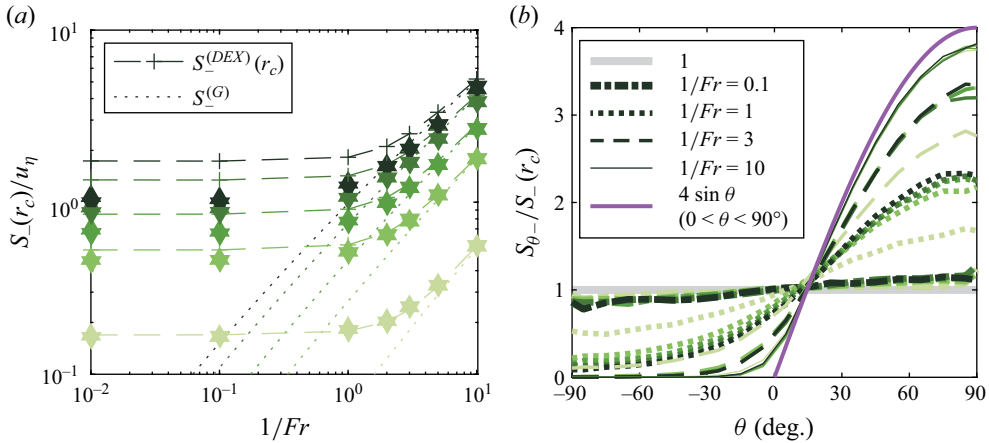


Figure 7. (a) Value of $S_-(r_c)$ at different $1/Fr$. The model predictions are displayed only for $Re_\lambda = 167$. The colour scheme and symbols follow figure 2(a). (b) The non-dimensionalised distribution of $S_{\theta-}$ along the polar angle θ for $Re_\lambda = 167$. The colour scheme follows figure 2(a).

4.3. Collision velocity

Besides the bubble–particle distribution, the collision kernel is determined by the effective radial approach velocity at collision distance $S_-(r_c)$ according to (1.3). Figure 7(a) shows $S_-(r_c)$ as a function of $1/Fr$. Here, S_- increases significantly with $1/Fr$ when $1/Fr > 1$ for all St and almost recovers the relative settling limit $S_-(^G)$ at $1/Fr \sim 10$ – a point which we will return to. At low $1/Fr$ where turbulence dominates, S_- differs across St because of the different collision mechanisms involved. At small St , collisions occur due to local fluid shear and the local turnstile effect, as introduced in § 1. As St increases, local effects become less important since the bubbles and particles interact with larger and more energetic eddies. Due to the different physical properties of bubbles and particles, the interaction is different between bubbles and particles, which contributes to S_- , i.e. the ‘non-local turnstile effect’. The local shear and local turnstile effects, as well as the relative settling effect of gravity, are properly represented in the extended Dodin & Elperin (2002) prediction $S_-(^{DEX})$, which explains its excellent agreement with the data throughout the entire $1/Fr$ range, at $St = 0.1$. However, it increasingly overpredicts S_- at larger St as it does not model any non-local effects. These non-local effects do not directly increase S_- by improving the alignment between the relative velocity vector and the separation vector, in contrast to the local turnstile effect. Considering only local effects at higher St regimes can therefore lead to the overprediction. At higher $1/Fr$, the overprediction decreases since the contribution of the turbulence collision mechanisms decreases and relative settling plays an increasingly dominant role. Another approach to quantify the gravity effect is to consider the angular distribution of $S_-(r_c)$ with respect to gravity, where $S_-(r_c)$ is binned using the polar angle θ around the bubble to obtain $S_{\theta-}$. This is plotted in figure 7(b) with $\theta = -90^\circ$ corresponding to the direction of gravity. In the no-gravity ($1/Fr = 0$) limit, there is no preferred direction and accordingly $S_{\theta-}$ is uniformly distributed across all θ (grey line). As $1/Fr$ increases, more and more collisions occur on the top half of a bubble where the approach velocity is enhanced due to gravitational settling and *vice versa* for the lower half. Consequently, the top hemisphere ($\theta > 0^\circ$) contributes more to $S_-(r_c)$ than the bottom one. This anisotropy is still very weak at $1/Fr = 0.1$ and becomes significant at $1/Fr = 1$, even though at this value $S_-(r_c)$ still has not increased significantly from the turbulence-dominated limit, as shown in figure 7(a).

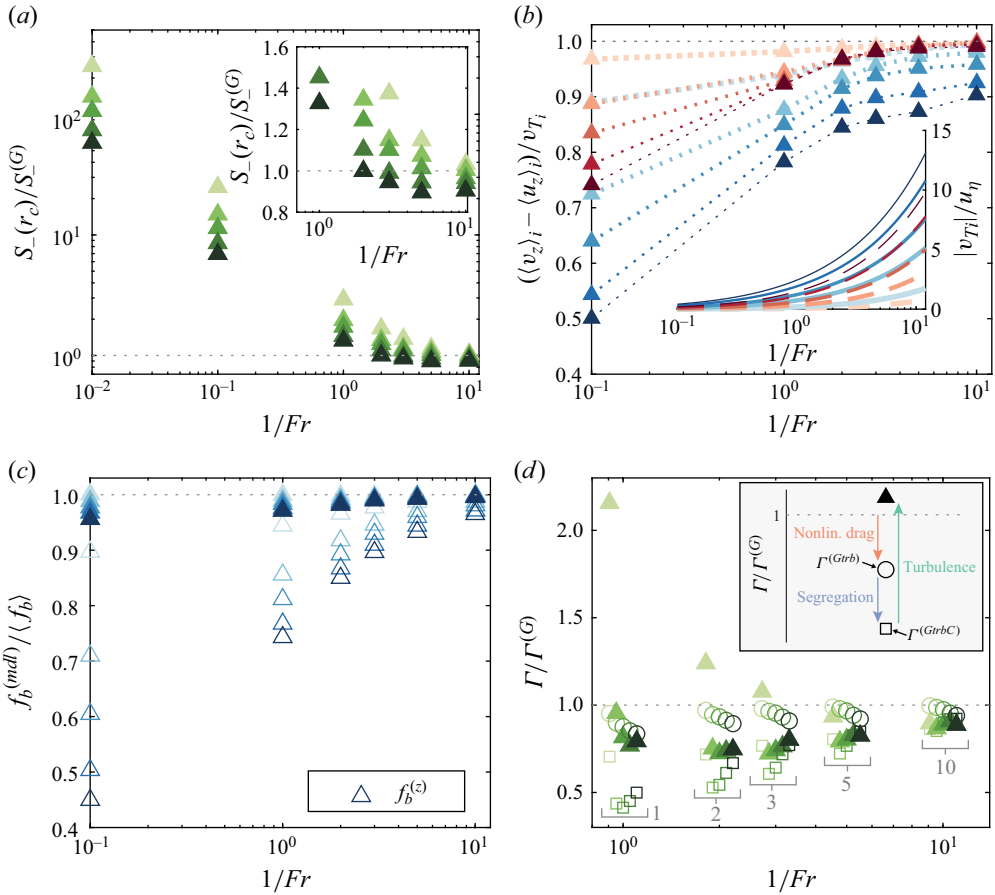


Figure 8. (a) The ratio of $S_-(r_c)$ to the relative settling case $S_-^{(G)}$ at $Re_\lambda = 167$. Inset shows an enlarged version of the region where $S_-(r_c) < S_-^{(G)}$. (b) The ratio of the average bubble and particle vertical slip velocity to the terminal velocity in still fluid accounting for nonlinear drag v_{Ti} , whose magnitude is shown in the inset (solid line for bubbles and dashed lines for particles), at $Re_\lambda = 167$. The lines in the main figure are guides for the eye. (c) The ratio of the modelled drag correction to the measured drag correction at $Re_\lambda = 167$. The open symbols indicate the drag correction based solely on the vertical slip velocity. (d) The collision kernel normalised by the relative settling case in still fluid at $Re_\lambda = 167$. Also shown are the relative settling collision kernel in turbulence $\Gamma^{(Grb)}$ and the effect of segregation. The cases with different St have been laterally displaced for clarity and the associated labels indicate the corresponding $1/Fr$. The symbols and the colour scheme in all the panels follow figures 2(a) and 4(a).

At $1/Fr = 10$, only a small fraction of the collisions occur in the bottom hemisphere due to turbulence, and the distribution is close to the relative settling limit (purple line) where collisions exclusively occur on the top hemisphere. Furthermore, in the range $1 \leq 1/Fr < 10$, $S_{\theta-}$ is not sensitive to St for $St \geq 0.5$, suggesting the transition from turbulence to relative settling for the collision velocity is similar at different values of St .

Similar to our analysis of the collision kernel, we normalise $S_-(r_c)$ with the relative settling case in still fluid $S_-^{(G)} = (|v_{Tb}| + |v_{Tp}|)/4$, where v_{Ti} are the terminal velocities obtained by balancing the drag and buoyancy terms in (3.2) taking $\mathbf{u} = \mathbf{0}$, and plot the result in figure 8(a). Although we only show the data for the $Re_\lambda = 167$ case, the results are not sensitive to Re_λ so the following discussion also applies to $Re_\lambda = 69$. Generally, $S_-(r_c)/S_-^{(G)}$ decreases as $1/Fr$ increases, reflecting the growing contribution of gravity.

Upon closer inspection, we observe that $S_-(r_c)$ for $St > 0.5$ dips below $S_-^{(G)}$, instead of simply approaching $S_-^{(G)}$ as is the case for $St = 0.1$. Note that this is not due to preferential sampling as the fluid velocities sampled by the colliding bubbles and particles are almost the same, as already shown in figure 4(b). To investigate why $S_- < S_-^{(G)}$, we compare the mean vertical slip velocity of the bubbles and particles $\langle v_z \rangle_i - \langle u_z \rangle_i$ with the theoretical terminal velocity in still fluid v_{Ti} , on which $S_-^{(G)}$ in figure 8(b) is based. For $St = 0.1$, $(\langle v_z \rangle_i - \langle u_z \rangle_i)/v_{Ti}$ is very close to 1 throughout, which is consistent with the fact that $S_- \geq S_-^{(G)}$. For higher St , however, the mean vertical slip velocity in turbulence is smaller than v_{Ti} . This effect is generally stronger for bubbles, more pronounced at high St and overall the ratio $(\langle v_z \rangle_i - \langle u_z \rangle_i)/v_{Ti}$ trends back up towards 1 as buoyancy becomes stronger. To understand its origin, we focus on the bubbles and consider the fact that turbulence induces additional horizontal slip velocities. As Re_i depends on magnitude of the total slip velocity, the horizontal slip increases the value of Re_i and the drag force, which can explain the slowdown (Ruth *et al.* 2021). To test this hypothesis, we model the slip velocity vector as $(\mathbf{v}_b - \mathbf{u})^{(mdl)} = (v_{bx} - u_{bx})' \mathbf{e}_x + (v_{bx} - u_{bx})' \mathbf{e}_y + (\langle v_z \rangle_b - \langle u_z \rangle_b) \mathbf{e}_z$, where $(v_{bx} - u_{bx})'$ is the measured r.m.s. of the horizontal bubble slip velocity and $\mathbf{e}_{x,y,z}$ are unit vectors along x -, y - and the vertical directions, respectively. Based on the magnitude of the slip velocity vector, we then calculate the resulting Re_i and the corresponding drag correction term $f_b^{(mdl)}$. Figure 8(c) shows that $f_b^{(mdl)}$ is indeed close to the measured mean drag correction $\langle f_b \rangle$. For reference, we also include the drag correction based on the vertical slip velocity only $(\mathbf{v}_b - \mathbf{u})^{(z)} = (\langle v_z \rangle_b - \langle u_z \rangle_b) \mathbf{e}_z$ as open symbols. As expected, $f_b^{(z)} < f_b^{(mdl)}$ and the difference reduces at larger $1/Fr$, consistent with the trend of $(\langle v_z \rangle_b - \langle u_z \rangle_b)/v_{Tb}$ in figure 8(b). This is because the mean vertical slip velocity becomes larger relative to the horizontal slip velocities with increasing $1/Fr$, such that $|\langle v_z \rangle_b - \langle u_z \rangle_b|$ increasingly dominates $|\mathbf{v}_b - \mathbf{u}|$. We therefore conclude that the observed reduction in the rise velocity is indeed due to enhanced nonlinear drag caused by the horizontal slip velocity components in turbulence.

Combining these insights, we re-examine the unexpected result that turbulence can reduce the collision rate (i.e. $\Gamma < \Gamma^{(G)}$), as seen in figure 2(a). Our analysis shows that this can be attributed to bubble–particle spatial segregation and the reduced bubble slip velocity in turbulence. To evaluate their respective importance, we again show $\Gamma/\Gamma^{(G)}$ in figure 8(d), this time focusing only on the parameter range where $\Gamma < \Gamma^{(G)}$. To quantify the effect of the nonlinear drag, we plot the relative settling collision kernel in turbulence $\Gamma^{(Gtrb)} = \pi r_c^2 [\langle v_z \rangle_b - \langle u_z \rangle_b - (\langle v_z \rangle_p - \langle u_z \rangle_p)]$, i.e. based on the measured vertical slip velocities of bubbles and particles. Here, $\Gamma^{(Gtrb)}/\Gamma^{(G)} \leq 1$ as the nonlinear drag reduces the bubble slip velocity. As $1/Fr$ increases, $\Gamma^{(Gtrb)}/\Gamma^{(G)}$ increases since the magnitude of the slip velocity is increasingly dominated by the vertical component, whereas $\Gamma^{(Gtrb)}/\Gamma^{(G)}$ decreases for increasing St as the effect of nonlinear drag becomes more pronounced. Since bubbles and particles segregate in turbulence, we also show $\Gamma^{(GtrbC)} = \Gamma^{(Gtrb)} \cdot g(r_c)$ in the figure. The difference between $\Gamma^{(GtrbC)}$ and $\Gamma^{(Gtrb)}$ decreases with increasing $1/Fr$, reflecting the fact that gravity reduces segregation. Finally, the difference between $\Gamma^{(GtrbC)}$ and Γ indicates the enhancement of the collision velocity due to turbulence mechanisms. This is larger at lower $1/Fr$ and by $1/Fr = 10$, $\Gamma \approx \Gamma^{(GtrbC)}$.

4.4. Effect of the particle density

In the previous sections, we fixed $\rho_p/\rho_f = 5$ and varied St and $1/Fr$. Nevertheless, ρ_p/ρ_f , which sets r_p hence r_c , can have an explicit effect on the particle dynamics

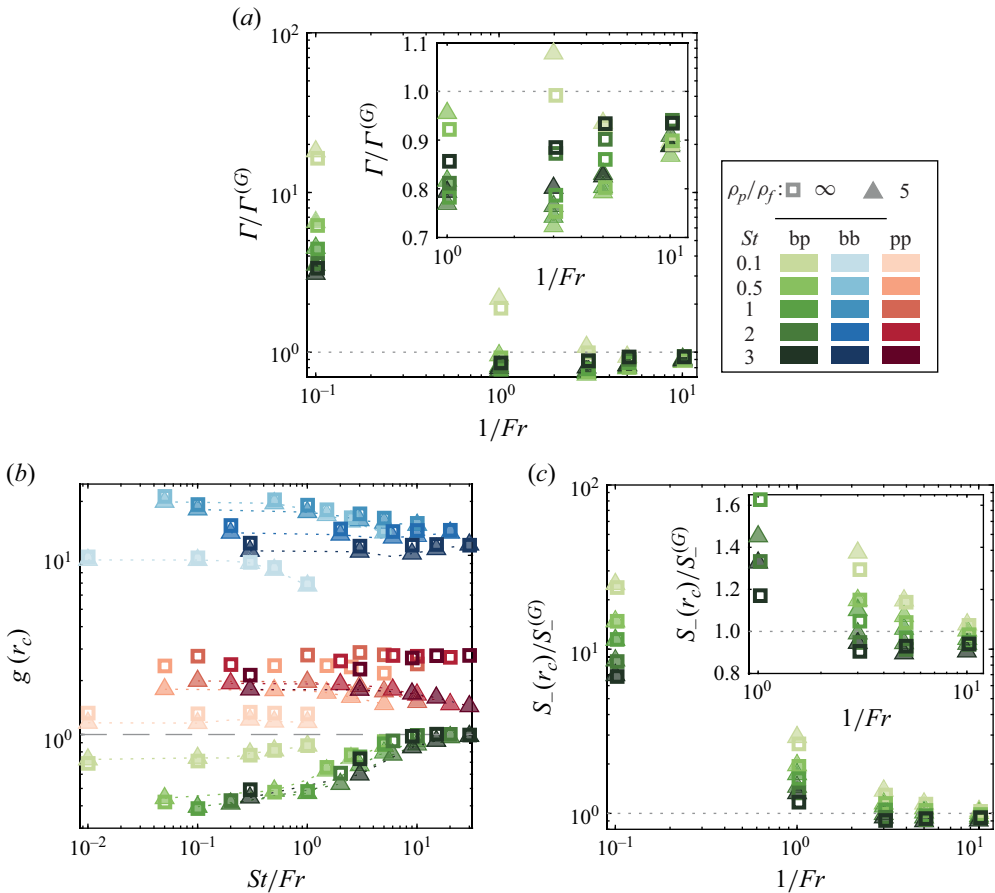


Figure 9. (a) The collision kernel Γ normalised by the relative settling limit, (b) the RDF $g(r_c)$ and (c) $S_-(r_c)$ normalised by the relative settling limit for both $\rho_p/\rho_b = 5$ (filled triangles) and $\rho_p/\rho_b = \infty$ (open squares) at $Re_\lambda = 167$. The insets in (a) and (c) are zooms in on the $1 \lesssim 1/Fr \lesssim 10$ region.

beyond determining the collision distance according to (3.2). We therefore additionally simulate $\rho_p/\rho_f = \infty$ with $1/Fr = 0.1, 1, 3, 5$ and 10 for all the tested values of St at $Re_\lambda = 167$, while retaining the same r_c as the $\rho_p/\rho_f = 5$ case. Figure 9 plots the collision kernel Γ , the RDF $g(r_c)$ and the effective radial approach velocity $S_-(r_c)$, in which Γ and $S_-(r_c)$ have been normalised by the relative settling limit to account for the different particle settling velocities. These data show that for the bubble–particle case neither the overall collision kernel $\Gamma/\Gamma^{(G)}$, nor the factors $g_{bp}(r_c)$ and $S_-(r_c)/S_-^{(G)}$, individually are sensitive to ρ_p . This is in contrast to the particle–particle case where $g_{pp}(r_c)$ remains constant or even increases slightly with $1/Fr$, which is shown in figure 9(b) and is also observed by Woittiez *et al.* (2009). Despite $g_{pp}(r_c)$ remaining above 1, $g_{bp}(r_c)$ approaches unity similar to the $\rho_p/\rho_f = 5$ case, which is consistent with our interpretation of figure 5(a) in § 4.2 that the trend in $g_{bp}(r_c)$ with $1/Fr$ is not principally due to a change in bubble or particle clustering strength. We furthermore note that, even for $\rho_p/\rho_f = \infty$, $S_-(r_c) < S_-^{(G)}$ and $\Gamma < \Gamma^{(G)}$ at intermediate values of $1/Fr$. This demonstrates that the reduction of the bubble–particle collision rate below the pure gravity case by turbulence is not specific to particles with $\rho_p/\rho_f = 5$.

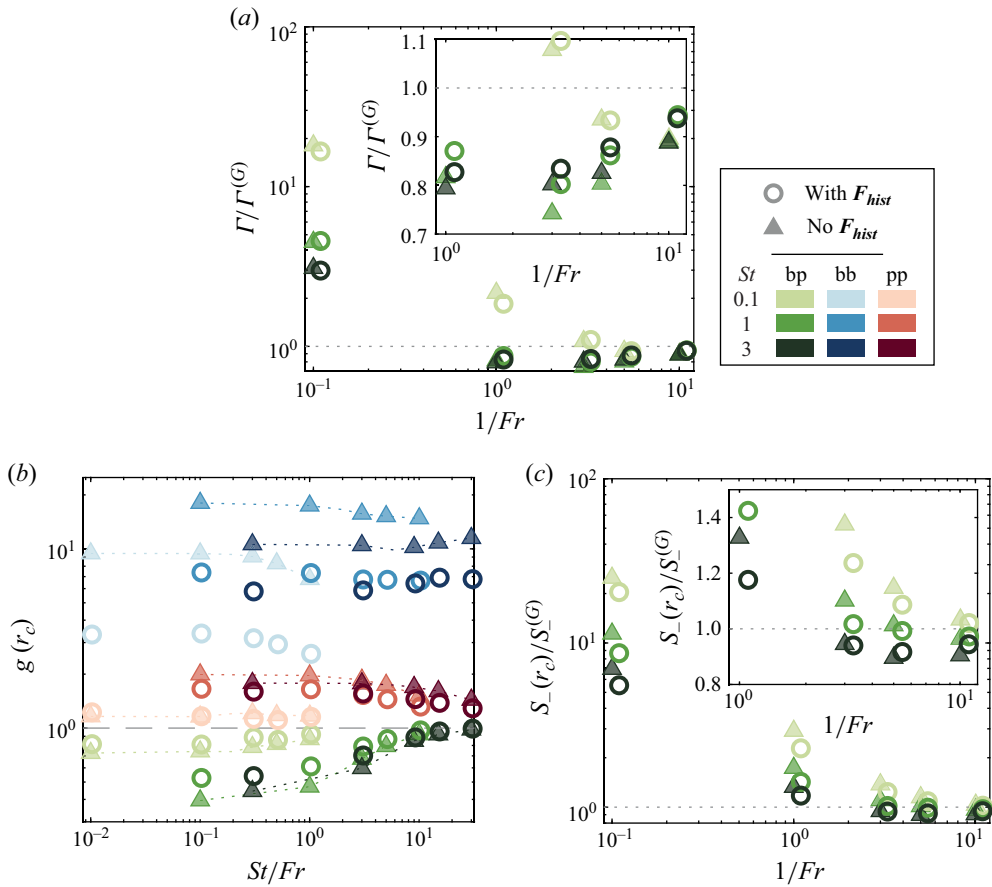


Figure 10. (a) The collision kernel Γ normalised by the relative settling limit, (b) the RDF $g(r_c)$ and (c) $S_-(r_c)$ normalised by the relative settling limit for the cases with and without the history force F_{hist} at $Re_\lambda = 167$. The insets in (a) and (c) are zooms in on the $1 \lesssim 1/Fr \lesssim 10$ region.

4.5. Effect of the history force

In addition to testing $\rho_p/\rho_f = \infty$, we examine the effect of the history force by including (3.3) in (3.2) and simulating $St = 0.1, 1$ and 3 for $1/Fr = 0.1, 1, 3, 5, 10$ at $Re_\lambda = 167$. The measured $\Gamma/\Gamma^{(G)}$, $g(r_c)$ and $S_-(r_c)/S_-^{(G)}$ are plotted in figure 10. These results show that the history force does not qualitatively change the bubble–particle collision statistics, insofar as the general trends with $1/Fr$ remain the same, the reduction of Γ and $S_-(r_c)$ below the relative settling limit is still observed in figures 10(a) and 10(c), and $g_{bp}(r_c)$ still lies below 1 at low to intermediate values of $1/Fr$, as shown by figure 10(b). Quantitatively, the history force does not significantly affect the collision kernel, since it tends to reduce $S_-(r_c)$ and increase the value of $g_{bp}(r_c)$. This increase in the value of $g_{bp}(r_c)$ towards 1 corresponds to reduced bubble–particle segregation. It is hence consistent with the lower values of $g_{bb}(r_c)$ and $g_{pp}(r_c)$ observed when the history force is included in figure 10(b), which indicate weaker bubble and particle clusters and have already been reported in the literature (Olivieri *et al.* 2014; Daitche 2015). In summary, our results show that the history force does not play a role in determining the qualitative trends of the bubble–particle collision statistics and only a minor one for the value of the collision kernel.

5. Discussion and conclusion

We studied the effect of gravity on bubble–particle collisions in HIT by conducting direct numerical simulations using the point-particle approach (Gatignol 1983; Maxey & Riley 1983; Auton 1987; Auton *et al.* 1988). From our simulations, we find that gravity is negligible and turbulence mechanisms determine the collision kernel up to $1/Fr = 0.1$. For instance, bubbles and particles form individual clusters and segregate in this regime. When $1 \lesssim 1/Fr < 10$, gravity noticeably influences the collision kernel even though the effects of turbulence are still significant. Gravity increases the collision kernel by reducing the extent of segregation and increasing the collision velocity since bubbles rise and particles settle. Notably, the collision kernel dips below the still fluid case when $1/Fr \gtrsim 5$ for $St = 0.1$ and $1/Fr \gtrsim 1$ for $St \geq 0.5$, meaning turbulence reduces the collision rate in this regime. This is due to preferential sampling and additionally for $St > 0.5$ a reduction in the bubble slip velocity due to nonlinear drag. Since both effects weaken as $1/Fr$ increases, turbulence effects become negligible and the collision kernel is well approximated by the still fluid case when $1/Fr \geq 10$. For our tested parameters, additional simulations reveal that the observed trends of the bubble–particle collision statistics are not sensitive to particle density and the history force. Quantitatively, the history force tends to reduce bubble–particle segregation and the effective bubble–particle radial approach velocity. These two phenomena have opposite effects on the collision kernel, such that the net effect of the history force on the collision kernel is weak. Although the existing bubble–particle collision models qualitatively capture the increasing trend in the collision velocity with $1/Fr$ over the tested range, none of them achieve quantitative agreement with the simulation data in terms of the collision kernel even when the predictions are appropriately compared with simulations without the history force. We extended the model by Dodin & Elperin (2002) to the bubble–particle case and found excellent agreement with our simulations over all $1/Fr$ for small St if segregation is accounted for and when the history force is neglected. Note that none of these models capture $S_- < S_-^{(G)}$, which occurs at higher St due to the effect of nonlinear drag. This leads to a discrepancy of up to 20% in S_- in the tested regime.

Throughout this paper, we have used both $1/Fr$ and St/Fr in order to parameterise the turbulence-to-gravity transition and the gravity-dominated limit. As discussed, gravity starts to play a noticeable role when $1/Fr \gtrsim 1$. To understand why $1/Fr$ is the relevant parameter, first take Δv as a proxy for S_- and consider the following heuristic argument: at small St , the bubble–particle relative velocity Δv is given by the shear mechanism which is $\propto \sqrt{St}$, the local turnstile mechanism which is $\propto St$, and the relative settling contribution which is $\propto St/Fr$ (see (B2)). Assuming the shear mechanism is weaker than the local turnstile mechanism, $\Delta v \propto St + St/Fr$. As $(\Delta v)/(\Delta v|_{1/Fr=0}) \propto 1 + 1/Fr$, we consider $1/Fr$ when examining the turbulence-to-gravity transition. On the other hand, St/Fr is the appropriate non-dimensional number for the gravity-dominant limit as relative settling is governed by St/Fr (Good *et al.* 2014).

Multiple questions still remain to be addressed. Our simulations are conducted using the point-particle approximation, which helps to provide a first-order appreciation of bubble–particle collisions and enables one-to-one comparison with the geometric collision models. As a trade-off for its relative simplicity, this approach limits access to the large- St regime and inherently neglects finite-size effects. For the largest values of St tested $r_b/\eta \sim 5$, which is beyond the commonly adopted bounds of the point-particle approximation (Homann & Bec 2010). Therefore, our results at these values should be interpreted with caution as finite-size effects may be relevant. Performing interface-resolved simulation using for example the immersed boundary method (Verzicco 2023)

can provide additional insights as the bubble distorts the local flow field and can further modify the bubble–particle distribution (Tiedemann & Fröhlich 2023; Jiang & Krug 2025), although the extra complexity would make it harder to distinguish whether the trends in the collision statistics are due to the locally deformed flow field or due to the background turbulence. Furthermore, we considered the more straightforward case of bubbles and particles with the same St . While this has provided much understanding into the collision process, unravelling the collision mechanisms for bubbles and particles with different St would prove invaluable for real life applications, where particles in flotation cells are usually far from monodispersed. In terms of modelling, a theoretical model of segregation will greatly enhance the predictive capabilities of the existing models.

Acknowledgements. We thank G. Piumini, D. van Buuren, K. Zhong and G. Vacca for helpful discussions.

Funding. This project has received funding from the European Research Council (ERC) under the European Union’s Horizon 2020 research and innovation programme (grant agreement No. 950111, BU-PACT). This work was carried out on the Dutch national e-infrastructure with the support of SURF Cooperative. We acknowledge the EuroHPC Joint Undertaking for awarding the project EHPC-REG-2023R03-178 access to the EuroHPC supercomputer Discoverer, hosted by Sofia Tech Park (Bulgaria).

Declaration of interests. The authors report no conflict of interest.

Data availability statement. All data supporting this study are openly available from the 4TU.ResearchData repository at <https://doi.org/10.4121/aac3a58a-67ea-4221-8ac0-48a66a5e960c>.

Appendix A. Consistent inclusion of gravity following Abrahamson (1975)

The original expression of the collision kernel including gravity as given in Abrahamson (1975) has an integration error which has been partly resolved by Kostoglou *et al.* (2020a) using a comparable expression. However, the equivalence between the expressions in Abrahamson (1975) and Kostoglou *et al.* (2020a) was not directly shown. We provide this additional detail in this appendix. Furthermore, we show the difference between (2.7) and the best-fit expressions reported in figure 2 and (10) in Kostoglou *et al.* (2020a).

According to Abrahamson (1975), the collision kernel between two types of particles in the presence of gravity is given by

$$\begin{aligned} \Gamma_{12} &= \pi r_c^2 v_c \\ &= \frac{\pi r_c^2}{(2\pi v_1^2)^{3/2} (2\pi v_2^2)^{3/2}} \int \int \int \int \int \int_{\text{all space}} \sqrt{(v_{1x} - v_{2x})^2 + (v_{1y} - v_{2y})^2 + (v_{1z} - v_{2z})^2} \\ &\quad \times \exp \left[\sum_{i=1}^2 -\frac{v_{ix}^2 + v_{iy}^2 + (v_{iz} - v_{Ti})^2}{2v_i^2} \right] dv_{1x} dv_{1y} dv_{1z} dv_{2x} dv_{2y} dv_{2z}, \end{aligned} \quad (\text{A1})$$

where the numerical subscripts 1, 2 denote the colliding particles, and the alphabetical subscripts x, y, z denote the corresponding velocity components. Changing variables such that $v_{iN} = v_{iz} - v_{Ti}$ for $i = 1, 2$ and further taking

$$v_{xm} = \frac{v_{1x} + v_{2x}}{2}, \quad v_{ym} = \frac{v_{1y} + v_{2y}}{2}, \quad v_{zm} = \frac{v_{1N} + v_{2N}}{2}, \quad (\text{A2a})$$

$$v_{xd} = v_{1x} - v_{2x}, \quad v_{yd} = v_{1y} - v_{2y}, \quad v_{zd} = v_{1N} - v_{2N}, \quad (\text{A2b})$$

yields

$$v_c = \frac{1}{(2\pi v_1'^2)^{3/2}(2\pi v_2'^2)^{3/2}} \iiint_{\text{all space}} \sqrt{v_{xd}^2 + v_{yd}^2 + [v_{zd} + (v_{T1} - v_{T2})]^2} \times I_x \cdot I_y \cdot I_z \cdot dv_{xd}dv_{yd}dv_{zd}, \tag{A3}$$

where

$$I_j = \int_{-\infty}^{+\infty} \exp \left[-\frac{v_1'^2 + v_2'^2}{2v_1'^2 v_2'^2} \left(v_{jm} - \frac{v_2'^2 - v_1'^2}{2(v_1'^2 + v_2'^2)} v_{jd} \right)^2 \right] \exp \left[-\frac{v_{jd}^2}{2(v_1'^2 + v_2'^2)} \right] dv_{jm}, \tag{A4}$$

and $j = x, y, z$. Using $\int_{-\infty}^{+\infty} \exp[-a(x - b)^2]dx = \sqrt{\pi/a}$ where a, b are constants to evaluate I_x, I_y and I_z

$$v_c = \frac{1}{[2\pi(v_1'^2 + v_2'^2)]^{3/2}} \iiint_{\text{all space}} \sqrt{v_{xd}^2 + v_{yd}^2 + [v_{zd} + (v_{T1} - v_{T2})]^2} \times \exp \left[-\frac{v_{xd}^2 + v_{yd}^2 + v_{zd}^2}{2(v_1'^2 + v_2'^2)} \right] dv_{xd}dv_{yd}dv_{zd}, \tag{A5}$$

which is the same as (8) in Kostoglou *et al.* (2020a) with the following mapping:

$$\sqrt{v_1'^2 + v_2'^2} \rightarrow V, \quad v_{T2} - v_{T1} \rightarrow U_B, \quad v_c \rightarrow U_T, \quad \frac{v_{T2} - v_{T1}}{\sqrt{v_1'^2 + v_2'^2}} \rightarrow \alpha, \quad \frac{v_c}{\sqrt{v_1'^2 + v_2'^2}} \rightarrow \Psi. \tag{A6}$$

Kostoglou *et al.* (2020a) numerically integrated (A5), showed a best-fit result in their figure 2 and stated in their (10) that the corresponding equation is

$$\frac{v_c}{\chi} = \begin{cases} 1.6, & \text{for } \alpha < 0.1 \\ -0.0181\alpha^3 + 0.213\alpha^2 - 0.1096\alpha + 1.584, & \text{for } 0.1 \leq \alpha \leq 5 \\ \alpha + (1/\alpha), & \text{for } \alpha > 5 \end{cases} \tag{A7}$$

where $\alpha = (v_{T2} - v_{T1})/\chi$ and $\chi = \sqrt{v_1'^2 + v_2'^2}$. Both the curve shown in their figure 2 and (A7) are plotted in figure 11, which clearly indicates their difference. We additionally include our best-fit expression (2.7), which shows excellent agreement with the numerical integration result as displayed in figure 2 of Kostoglou *et al.* (2020a).

Appendix B. Extension of the Dodin & Elperin (2002) model to particles with different densities

The Dodin & Elperin (2002) model is applicable for infinitely heavy inertial particles with a uniform spatial distribution in HIT. Here, we extend it to particles with different densities by incorporating the density ratio $\beta_i = 2(\rho_f - \rho_i)/(\rho_f + 2\rho_i)$.

We start from (3.2) in the small St limit without lift (Fouxon 2012)

$$\mathbf{v}_i = \mathbf{u} + \frac{\beta_i \tau_i}{f_i} \boldsymbol{\psi} + \frac{\beta_i \tau_i}{f_i} \mathbf{g} \mathbf{e}_z, \tag{B1}$$

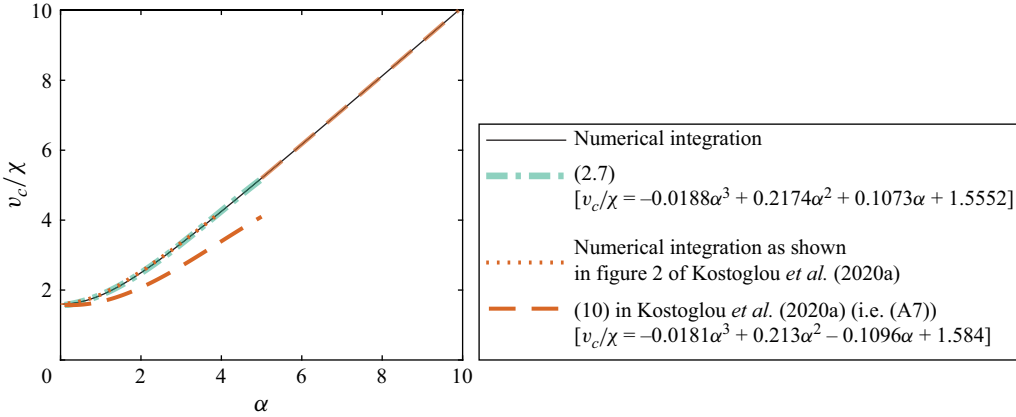


Figure 11. Plot of v_c/χ as a function of α . Note that (2.7) differs from (A7) as the fitting coefficients are different for $0.1 \leq \alpha \leq 5$. The respective fits in this range are displayed in the legend.

where $\psi = Du/Dt$. Consider the case where two particles located at positions A and B are at collision distance such that their separation is small. Here, $\psi|_A \approx \psi|_B$ and

$$\Delta \mathbf{v} = \mathbf{v}_2 - \mathbf{v}_1 = \underbrace{(\mathbf{u}|_B - \mathbf{u}|_A)}_{\Delta \mathbf{v}_f} + \underbrace{\left(\frac{\beta_2 \tau_2}{f_2} - \frac{\beta_1 \tau_1}{f_1} \right) \psi|_A}_{\Delta \mathbf{v}_g} + \left(\frac{\beta_2 \tau_2}{f_2} - \frac{\beta_1 \tau_1}{f_1} \right) \mathbf{g} \mathbf{e}_z, \quad (\text{B2})$$

in which $\Delta \mathbf{v}$ has been split into fluid $\Delta \mathbf{v}_f$ and gravity contributions $\Delta \mathbf{v}_g$. Projecting (B2) along the separation vector, of which \mathbf{e}_r is the corresponding unit vector, gives

$$\Delta v_r(\theta) = (\Delta \mathbf{v}_f + \Delta \mathbf{v}_g) \cdot \mathbf{e}_r := \xi + h(\theta) = \xi + \left(\frac{\beta_2 \tau_2}{f_2} - \frac{\beta_1 \tau_1}{f_1} \right) g \cos \theta. \quad (\text{B3})$$

As the background flow is HIT, ξ is isotropic so it is assumed to be normally distributed. Furthermore, since $h(\theta)$ has a sign ambiguity originating from the possibility of labelling either particle as number 1, we introduce

$$h_+(\theta) = \left| \frac{\beta_2 \tau_2}{f_2} - \frac{\beta_1 \tau_1}{f_1} \right| g \cos \theta, \quad (\text{B4})$$

and write

$$\begin{aligned} \langle |\Delta v_r(\theta)| \rangle &= \int_{-\infty}^{+\infty} \frac{|\alpha|}{\sigma \sqrt{2\pi}} \exp\left(-\frac{(\alpha - h_+)^2}{2\sigma^2}\right) d\alpha \\ &= \sigma \sqrt{2} \kappa \operatorname{erf} \kappa + \sigma \sqrt{\frac{2}{\pi}} \exp(-\kappa^2), \end{aligned} \quad (\text{B5})$$

where $\langle \cdot \rangle$ denotes averaging, $\kappa = h_+(\sigma \sqrt{2})$ and $\sigma = \sqrt{\langle \xi^2 \rangle} = \sigma_{\Delta v_r}^{(DEX)}$ is the r.m.s. of ξ (we drop the subscript and superscript of $\sigma_{\Delta v_r}^{(DEX)}$ in this appendix to reduce clutter). For σ , we use the isotropy of the background flow and place particle 2 along the x -axis at position C. Similar to before, we consider particles at collision distance so $\psi|_A \approx \psi|_C$, meaning

$$\begin{aligned} \sigma^2 &= \langle \xi^2 \rangle = \langle (\Delta \mathbf{v}_f \cdot \mathbf{e}_x)^2 \rangle \\ &= \langle (u_x|_C - u_x|_A)^2 \rangle + \left(\frac{\beta_2 \tau_2}{\langle f_2 \rangle} - \frac{\beta_1 \tau_1}{\langle f_1 \rangle} \right)^2 \langle \psi_x^2|_A \rangle \\ &\quad + 2 \left(\frac{\beta_2 \tau_2}{\langle f_2 \rangle} - \frac{\beta_1 \tau_1}{\langle f_1 \rangle} \right) \langle (u_x|_C - u_x|_A) \psi_x|_A \rangle, \end{aligned} \quad (\text{B6})$$

where $\psi_x = Du_x/Dt$. Additionally, as $\langle (u_x|_C - u_x|_A) \psi_x|_A \rangle \approx \langle (u_x|_C - u_x|_A) \psi_x|_C \rangle = -\langle (u_x|_C - u_x|_A) \psi_x|_A \rangle$ due to homogeneity, $\langle (u_x|_C - u_x|_A) \psi_x|_A \rangle \approx 0$. Therefore,

$$\sigma^2 = r_c^2 \left\langle \left(\frac{\partial u_x}{\partial x} \right)^2 \right\rangle + \left(\frac{\beta_2 \tau_2}{\langle f_2 \rangle} - \frac{\beta_1 \tau_1}{\langle f_1 \rangle} \right)^2 \left\langle \left(\frac{Du_x}{Dt} \right)^2 \right\rangle := r_c^2 \gamma^2 + \left(\frac{\beta_2 \tau_2}{\langle f_2 \rangle} - \frac{\beta_1 \tau_1}{\langle f_1 \rangle} \right)^2 \lambda^2, \quad (\text{B7})$$

where $\gamma^2 = \langle (\partial u_x / \partial x)^2 \rangle = \varepsilon / (15\nu)$ and $\lambda^2 = \langle (Du_x / Dt)^2 \rangle = 1.3\varepsilon^{3/2} \nu^{-1/2}$.

Finally, note that, in the case where $g(r_c) = 1$,

$$\Gamma_{12} = \frac{1}{2} \int_0^\pi \langle |\Delta v_r(\theta)| \rangle (2\pi r_c \sin \theta) r_c d\theta = \pi r_c^2 \int_0^\pi \langle |\Delta v_r(\theta)| \rangle \sin \theta d\theta, \quad (\text{B8})$$

where the factor 1/2 in the first equality singles out the inward flux of particles across the collision sphere assuming flux balance. This equation can be further simplified using symmetry of $\langle |\Delta v_r(\theta)| \rangle$

$$\langle |\Delta v_r(\pi - \theta)| \rangle = \langle |\xi - h(\theta)| \rangle = \langle |-\xi + h(\theta)| \rangle = \langle |\Delta v_r(\theta)| \rangle, \quad (\text{B9})$$

where the final equality is attributed to the symmetry of the distribution of ξ about 0. Equation (B8) then becomes

$$\Gamma_{12} = 2\pi r_c^2 \int_0^{\pi/2} \langle |\Delta v_r(\theta)| \rangle \sin \theta d\theta. \quad (\text{B10})$$

Performing the integration results in

$$\Gamma_{12} = \sqrt{8\pi} r_c^2 \sigma f(c), \quad (\text{B11})$$

where

$$f(c) = \frac{\sqrt{\pi}}{2} \left(c + \frac{1}{2c} \right) \text{erfc} + \frac{\exp(-c^2)}{2}, \quad (\text{B12})$$

and

$$c = \frac{|\beta_2 \tau_2 / \langle f_2 \rangle - \beta_1 \tau_1 / \langle f_1 \rangle| g}{\sqrt{2}\sigma}. \quad (\text{B13})$$

Appendix C. Domain size effects

The simulations reported are conducted in a cubic domain with $L_{\text{box}} = 1$. With gravity, bubble and particle statistics may exhibit periodicity effects if the time taken by the bubbles and particles to travel through the periodic simulation domain is less than the eddy turnover time, i.e. $T_{\text{box},i} < \ell / u'$ (Woittiez *et al.* 2009), where ℓ is the integral length scale. Taking $T_{\text{box},i} \sim L_{\text{box},z} / |\beta_i| \tau_i g$, this means

$$\max(St_i) = Fr \cdot \frac{L_{\text{box},z} u'}{\ell u_\eta |\beta_i|}, \quad (\text{C1})$$

	$Re_\lambda = 69$							$Re_\lambda = 167$						
$1/Fr$	0.01	0.1	1	2	3	5	10	0.01	0.1	1	2	3	5	10
$\max(St_b)$	1947.2	194.7	19.5	9.7	6.5	3.9	1.9	3217.7	321.8	32.2	16.1	10.7	6.4	3.2
$\max(St_p)$	5338.5	533.9	53.4	26.7	17.8	10.7	5.3	8821.7	882.2	88.2	44.1	29.4	17.6	8.8

Table 2. The maximum St that satisfies the criterion in (C1) when $L_{boxz} = 1$.

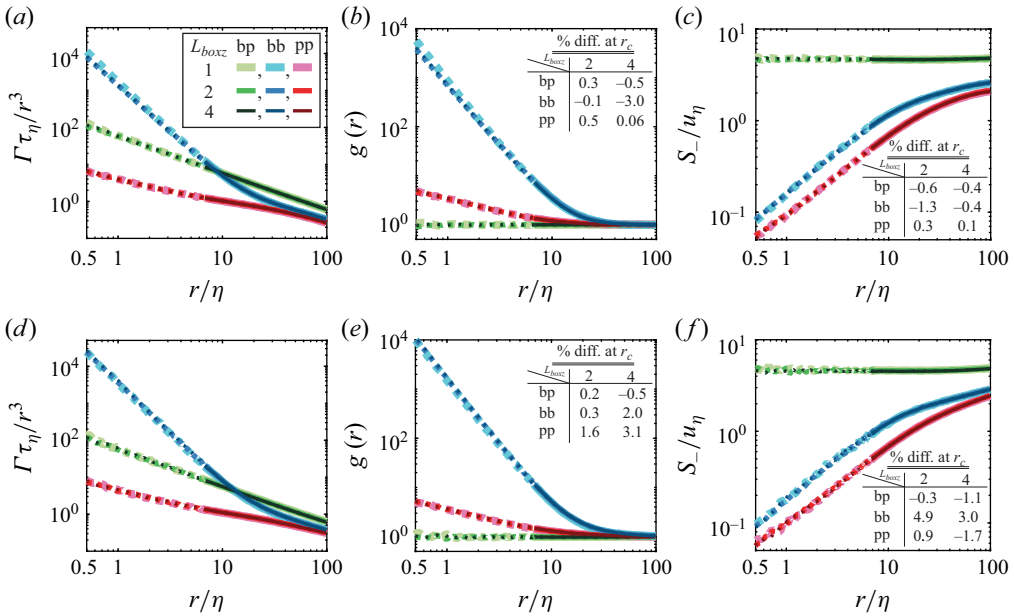


Figure 12. The (a) collision kernel, (b) RDF and (c) effective radial approach velocity with different L_{boxz} at $Re_\lambda = 69$ and (d-f) $Re_\lambda = 167$. The dotted segments indicate $r < r_c$. The tables in (b-c) and (e-f) show the percentage difference of the values at r_c compared with the $L_{boxz} = 1$ case.

where L_{boxz} is the vertical domain size. Table 2 shows that the maximum St is not exceeded with $L_{boxz} = 1$ even for the largest St_b and St_p simulated except for the $(Re_\lambda, 1/Fr) = (69, 10)$ case. To confirm the collision statistics are not affected even then, we lengthen the simulation domain along the vertical direction following Chouippe & Uhlmann (2015) and rerun the $(St, 1/Fr) = (3, 10)$ cases. Figure 12 shows that $\Gamma(r)$, $g(r)$ and $S_-(r)$ are not sensitive to L_{boxz} for bubble–particle, bubble–bubble and particle–particle collisions.

Appendix D. Code verification

The code used in this study is identical to the already verified code used in Chan *et al.* (2023) apart from the addition of the buoyancy, history force and lift terms. To verify the buoyancy term, we first omit the history force and simulate 100 bubbles rising in still fluid. Figure 13(a) shows that their terminal rise velocities correspond to the theoretical value ($v_T = 0.117$). We next add the history force and consider a particle settling in still fluid. Here, we employ Stokes drag ($f_p = 1$) to enable comparison with the analytical solution of the velocity time series by van Hinsberg *et al.* (2011). As shown in figure 13(a), the

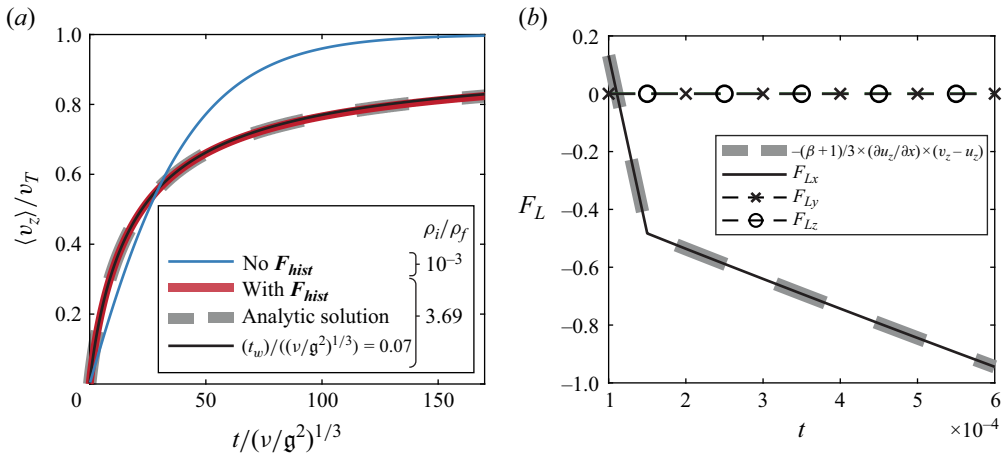


Figure 13. (a) Time series of the mean vertical velocity of 100 bubbles rising in quiescent liquid (blue line) with a Galileo number $Ga_b = \sqrt{g(2r_b)^3|\rho_b/\rho_f - 1|}/\nu = 106$, $\rho_b/\rho_f = 1/1000$ and nonlinear drag $f_b = 1 + 0.169Re_b^{2/3}$, as well as that of a particle settling in quiescent liquid with $Ga_p = 36$, $\rho_p/\rho_f = 3.69$ and Stokes drag $f_p = 1$. (b) The lift force acting on a bubble with $(Ga_b, \rho_b/\rho_f) = (106, 1/1000)$ and nonlinear drag $f_b = 1 + 0.169Re_b^{2/3}$ in a simple shear flow.

numerical and analytic solutions agree perfectly when the window length of the history force spans the entire simulation duration, and the agreement is still excellent if a window length of $t_w/(v/g^2)^{1/3} = 0.07$, which corresponds to 5 time steps, is used.

For the lift term, we checked that the lift force acting on a bubble in a simple shear flow with $\partial u_z/\partial x = 0.64$ is equal to the manually computed value given by the lift force expression in figure 13(b).

REFERENCES

- ABRAHAMSON, J. 1975 Collision rates of small particles in a vigorously turbulent fluid. *Chem. Eng. Sci.* **30** (11), 1371–1379.
- AHMED, N. & JAMESON, G.J. 1985 The effect of bubble size on the rate of flotation of fine particles. *Intl J. Miner. Process.* **14** (3), 195–215.
- AUTON, T.R. 1987 The lift force on a spherical body in a rotational flow. *J. Fluid Mech.* **183**, 199–218.
- AUTON, T.R., HUNT, J.C.R. & PRUD’HOMME, M. 1988 The force exerted on a body in inviscid unsteady non-uniform rotational flow. *J. Fluid Mech.* **197**, 241–257.
- BEC, J., HOMANN, H. & RAY, S.S. 2014 Gravity-driven enhancement of heavy particle clustering in turbulent flow. *Phys. Rev. Lett.* **112** (18), 184501.
- BLOOM, F. & HEINDEL, T.J. 2002 On the structure of collision and detachment frequencies in flotation models. *Chem. Eng. Sci.* **57** (13), 2467–2473.
- CALZAVARINI, E., CENCINI, M., LOHSE, D. & TOSCHI, F. 2008 Quantifying turbulence-induced segregation of inertial particles. *Phys. Rev. Lett.* **101** (8), 084504.
- CALZAVARINI, E., VOLK, R., LÉVÊQUE, E., PINTON, J.-F. & TOSCHI, F. 2012 Impact of trailing wake drag on the statistical properties and dynamics of finite-sized particle in turbulence. *Physica D* **241** (3), 237–244.
- CHAN, T.T.K., NG, C.S. & KRUG, D. 2023 Bubble–particle collisions in turbulence: insights from point-particle simulations. *J. Fluid Mech.* **959**, A6.
- CHOUIPPE, A. & UHLMANN, M. 2015 Forcing homogeneous turbulence in direct numerical simulation of particulate flow with interface resolution and gravity. *Phys. Fluids* **27** (12), 123301.
- DAITCHE, A. 2015 On the role of the history force for inertial particles in turbulence. *J. Fluid Mech.* **782**, 567–593.
- DHARIWAL, R. & BRAGG, A.D. 2018 Small-scale dynamics of settling, bidisperse particles in turbulence. *J. Fluid Mech.* **839**, 594–620.

- DODIN, Z. & ELPERIN, T. 2002 On the collision rate of particles in turbulent flow with gravity. *Phys. Fluids* **14** (8), 2921–2924.
- DORGAN, A.J. & LOTH, E. 2007 Efficient calculation of the history force at finite Reynolds numbers. *Intl J. Multiphase Flow* **33** (8), 833–848.
- ESWARAN, V. & POPE, S.B. 1988 An examination of forcing in direct numerical simulations of turbulence. *Comput. Fluids* **16** (3), 257–278.
- FALKINHOFF, F., OBLIGADO, M., BOURGOIN, M. & MININNI, P.D. 2020 Preferential concentration of free-falling heavy particles in turbulence. *Phys. Rev. Lett.* **125** (6), 064504.
- FARROKHPAY, S., FILIPPOV, L. & FORNASIERO, D. 2021 Flotation of fine particles: a review. *Miner. Process. Extr. Metall. Rev.* **42** (7), 473–483.
- FOUXON, I. 2012 Distribution of particles and bubbles in turbulence at a small Stokes number. *Phys. Rev. Lett.* **108** (13), 134502.
- GATIGNOL, R. 1983 The Faxén formulas for a rigid particle in an unsteady non-uniform Stokes flow. *J. Méc. Théor. Appl* **2** (2), 143–160.
- GOOD, G.H., IRELAND, P.J., BEWLEY, G.P., BODENSCHATZ, E., COLLINS, L.R. & WARHAFT, Z. 2014 Settling regimes of inertial particles in isotropic turbulence. *J. Fluid Mech.* **759**, R3.
- GUALTIERI, P., PICANO, F. & CASCIOLA, C.M. 2009 Anisotropic clustering of inertial particles in homogeneous shear flow. *J. Fluid Mech.* **629**, 25–39.
- VAN HINSBERG, M.A.T., TEN THIJE BOONKAMP, J.H.M. & CLERCX, H.J.H. 2011 An efficient, second order method for the approximation of the Basset history force. *J. Comput. Phys.* **230** (4), 1465–1478.
- VAN HINSBERG, M.A.T., TEN THIJE BOONKAMP, J.H.M., TOSCHI, F. & CLERCX, H.J.H. 2013 Optimal interpolation schemes for particle tracking in turbulence. *Phys. Rev. E* **87** (4), 043307.
- HOMANN, H. & BEC, J. 2010 Finite-size effects in the dynamics of neutrally buoyant particles in turbulent flow. *J. Fluid Mech.* **651**, 81–91.
- IRELAND, P.J., BRAGG, A.D. & COLLINS, L.R. 2016a The effect of Reynolds number on inertial particle dynamics in isotropic turbulence. Part 1. Simulations without gravitational effects. *J. Fluid Mech.* **796**, 617–658.
- IRELAND, P.J., BRAGG, A.D. & COLLINS, L.R. 2016b The effect of Reynolds number on inertial particle dynamics in isotropic turbulence. Part 2. Simulations with gravitational effects. *J. Fluid Mech.* **796**, 659–711.
- JIANG, L. & KRUG, D. 2025 How turbulence increases the bubble–particle collision rate. *J. Fluid Mech.* **1006**, A19.
- JIMÉNEZ, J., WRAY, A.A., SAFFMAN, P.G. & ROGALLO, R.S. 1993 The structure of intense vorticity in isotropic turbulence. *J. Fluid Mech.* **255**, 65–90.
- KOH, P.T.L., MANICKAM, M. & SCHWARZ, M.P. 2000 CFD simulation of bubble–particle collisions in mineral flotation cells. *Miner. Eng.* **13** (14), 1455–1463.
- KOH, P.T.L. & SCHWARZ, M.P. 2006 CFD modelling of bubble–particle attachments in flotation cells. *Miner. Eng.* **19** (6), 619–626.
- KOSTOGLU, M., KARAPANTSIOS, T.D. & EVGENIDIS, S. 2020a On a generalized framework for turbulent collision frequency models in flotation: The road from past inconsistencies to a concise algebraic expression for fine particles. *Adv. Colloid Interface Sci.* **284**, 102270.
- KOSTOGLU, M., KARAPANTSIOS, T.D. & OIKONOMIDOU, O. 2020b A critical review on turbulent collision frequency/efficiency models in flotation: Unravelling the path from general coagulation to flotation. *Adv. Colloid Interface Sci.* **279**, 102158.
- LEGENDRE, D. & MAGNAUDET, J. 1998 The lift force on a spherical bubble in a viscous linear shear flow. *J. Fluid Mech.* **368**, 81–126.
- MAGNAUDET, J. & LEGENDRE, D. 1998 Some aspects of the lift force on a spherical bubble. *Appl. Sci. Res.* **58** (1), 441–461.
- MATHAI, V., LOHSE, D. & SUN, C. 2020 Bubbly and buoyant particle–laden turbulent flows. *Annu. Rev. Condens. Matt. Phys.* **11** (1), 529–559.
- MAXEY, M.R. 1987 The gravitational settling of aerosol particles in homogeneous turbulence and random flow fields. *J. Fluid Mech.* **174**, 441–465.
- MAXEY, M.R. & RILEY, J.J. 1983 Equation of motion for a small rigid sphere in a nonuniform flow. *Phys. Fluids* **26** (4), 883–889.
- MAZZITELLI, I.M. & LOHSE, D. 2004 Lagrangian statistics for fluid particles and bubbles in turbulence. *New J. Phys.* **6** (1), 203–203.
- MAZZITELLI, I.M., LOHSE, D. & TOSCHI, F. 2003 The effect of microbubbles on developed turbulence. *Phys. Fluids* **15** (1), L5–L8.
- MICHAELIDES, E.E. 2003 Hydrodynamic force and heat/mass transfer from particles, bubbles, and drops—the Freeman scholar lecture. *J. Fluids Eng.* **125** (2), 209–238.

- MIETTINEN, T., RALSTON, J. & FORNASIERO, D. 2010 The limits of fine particle flotation. *Miner. Eng.* **23** (5), 420–437.
- NGO-CONG, D., NGUYEN, A.V. & TRAN-CONG, T. 2018 Isotropic turbulence surpasses gravity in affecting bubble-particle collision interaction in flotation. *Miner. Eng.* **122**, 165–175.
- NGUYEN, A.V. & SCHULZE, H.J. 2004 *Colloidal science of flotation*. In *Surfactant Sciences*. 1st edn, vol. 118. CRC Press.
- OLIVIERI, S., PICANO, F., SARDINA, G., IUDICONE, D. & BRANDT, L. 2014 The effect of the Basset history force on particle clustering in homogeneous and isotropic turbulence. *Phys. Fluids* **26** (4), 041704.
- PARISHANI, H., AYALA, O., ROSA, B., WANG, L.-P. & GRABOWSKI, W.W. 2015 Effects of gravity on the acceleration and pair statistics of inertial particles in homogeneous isotropic turbulence. *Phys. Fluids* **27** (3), 033304.
- PUMIR, A. & WILKINSON, M. 2016 Collisional aggregation due to turbulence. *Annu. Rev. Condens. Matt. Phys.* **7** (1), 141–170.
- RUTH, D.J., VERNET, M., PERRARD, S. & DEIKE, L. 2021 The effect of nonlinear drag on the rise velocity of bubbles in turbulence. *J. Fluid Mech.* **924**, A2.
- SAFFMAN, P.G. & TURNER, J.S. 1956 On the collision of drops in turbulent clouds. *J. Fluid Mech.* **1** (1), 16–30.
- TIEDEMANN, B. & FRÖHLICH, J. 2023 Collision dynamics of particles and bubbles in gravity-driven flotation: a DNS investigation. *PAMM* **23** (3), e202300290.
- VERZICCO, R. 2023 Immersed boundary methods: historical perspective and future outlook. *Annu. Rev. Fluid Mech.* **55** (1), 129–155.
- VOSSKUHL, M., PUMIR, A., LÉVÊQUE, E. & WILKINSON, M. 2014 Prevalence of the sling effect for enhancing collision rates in turbulent suspensions. *J. Fluid Mech.* **749**, 841–852.
- WAN, D., YI, X., WANG, L.-P., SUN, X., CHEN, S. & WANG, G. 2020 Study of collisions between particles and unloaded bubbles with point-particle model embedded in the direct numerical simulation of turbulent flows. *Miner. Eng.* **146**, 106137.
- WANG, L.-P. & MAXEY, M.R. 1993 Settling velocity and concentration distribution of heavy particles in homogeneous isotropic turbulence. *J. Fluid Mech.* **256**, 27–68.
- WANG, L.-P., WEXLER, A.S. & ZHOU, Y. 1998 On the collision rate of small particles in isotropic turbulence. I. Zero-inertia case. *Phys. Fluids* **10** (1), 266–276.
- WOITTEZ, E.J.P., JONKER, H.J.J. & PORTELA, L.M. 2009 On the combined effects of turbulence and gravity on droplet collisions in clouds: a numerical study. *J. Atmos. Sci.* **66** (7), 1926–1943.
- YUU, S. 1984 Collision rate of small particles in a homogeneous and isotropic turbulence. *AIChE J.* **30** (5), 802–807.